

The impact of gas disc flaring on rotation curve decomposition and revisiting baryonic and dark-matter relations for nearby galaxies

Pavel E. Mancera Piña^{1,2*}, Filippo Fraternali¹, Tom Oosterloo^{2,1}, Elizabeth A. K. Adams^{2,1}, Enrico di Teodoro^{3,4}, Cecilia Bacchini⁵, and Giuliano Iorio^{5,6}

¹ Kapteyn Astronomical Institute, University of Groningen, Landleven 12, 9747 AD, Groningen, The Netherlands

² ASTRON, Netherlands Institute for Radio Astronomy, Postbus 2, 7900 AA Dwingeloo, The Netherlands

³ Department of Physics & Astronomy, Johns Hopkins University, Baltimore, MD 21218, USA

⁴ Space Telescope Science Institute, 3700 San Martin Drive, Baltimore, MD 21218, USA

⁵ INAF-Osservatorio Astronomica di Padova, Vicolo dell'Osservatorio 5, I-35122 Padova, Italy

⁶ Physics and Astronomy Department Galileo Galilei, University of Padova, Vicolo dell'Osservatorio 3, I-35122, Padova, Italy

27 May 2022

ABSTRACT

Gas discs of late-type galaxies are flared, with scale heights increasing with the distance from the galaxy centres and often reaching kpc scales. We study the effects of gas disc flaring on the recovered dark matter halo parameters from rotation curve decomposition. For this, we carefully select a sample of 32 dwarf and spiral galaxies with high-quality neutral gas, molecular gas, and stellar mass profiles, robust H I rotation curves obtained via 3D kinematic modelling, and reliable bulge-disc decomposition. By assuming vertical hydrostatic equilibrium, we derive the scale heights of the atomic and molecular gas discs and fit dark matter haloes to the rotation curves self-consistently. We find that the effect of the gas flaring in the rotation curve decomposition can play an important role only for the smallest, gas-dominated dwarfs, while for most of the galaxies the effect is minor and can be ignored. We revisit the stellar– and baryon–to–halo mass relations ($M_* - M_{200}$ and $M_{\text{bar}} - M_{200}$). Both relations increase smoothly up to $M_{200} \approx 10^{12} M_\odot$, with galaxies at this end having high M_*/M_{200} and M_{bar}/M_{200} ratios approaching the cosmological baryon fraction. At higher M_{200} the relations show a larger scatter. Most haloes of our galaxy sample closely follow the concentration–mass ($c_{200} - M_{200}$) relation resulting from N-body cosmological simulations. Interestingly, the galaxies deviating above and below the relation have the highest and lowest stellar and baryon fractions, respectively, which suggests that the departures from the $c_{200} - M_{200}$ law are regulated by adiabatic contraction and an increasing importance of feedback.

Key words: galaxies: evolution – galaxies: fundamental parameters – galaxies: kinematics and dynamics – galaxies: ISM – galaxies: structure – cosmology: dark matter

1 INTRODUCTION

About 50 years have passed since the first set of works aiming to use rotation curve decomposition to study, and provide evidence for, the dark matter content of galaxies (e.g. Freeman 1970; Roberts & Rots 1973; Shostak 1973; Bosma 1978; Rubin et al. 1980; van Albada & Sancisi 1986; Begeman 1987, see also Bertone & Hooper 2018 for a historical review). The main idea is well known: provided the distribution of stars and gas within a galaxy, one can compare the contribution from these baryonic components to the gravitational potential against the total potential traced by the observed rotation curve of the galaxy, and infer the mass distribution of the host dark matter halo. Significant work has also been done using rotation curves decomposition to test alternative theories to dark matter (e.g. Milgrom 1983; Kent 1987; McGaugh & de Blok 1998; Famaey & McGaugh 2012).

The derivation of mass models has become significantly more accurate and detailed than in the first studies half a century ago. Nowadays, mass models use high quality data with high resolution kinematic measurements (typically H I data) and accurate near-IR photometry to study the dynamics of relatively large galaxy samples (e.g. de Blok et al. 2008; Frank et al. 2016; Lelli et al. 2016a), using robust statistical techniques such as Bayesian inference (e.g. Read et al. 2016b; Posti et al. 2019), and testing a variety of dark matter haloes and even different types of dark matter (e.g. Ren et al. 2019; Li et al. 2020; Zentner et al. 2022). These models are used on a daily basis for a variety of applications on galaxy evolution and near-field cosmology.

A limitation of almost all the mass models available in the literature, is that they assume that the gas (and sometimes also the stars) is distributed in razor-thin discs. Yet, it has been well established observationally that gas discs are not only thick, but they are also flared, with a scale height increasing with galactocentric distance, as

* e-mail: pavel@astro.rug.nl

expected for systems in vertical hydrostatic equilibrium (e.g. [Romeo 1992](#); [Olling 1995](#); [Yim et al. 2014](#); [Cimatti et al. 2019](#)).

Other than in the Milky Way (e.g. [Nakanishi & Sofue 2003](#); [Kalberla & Dedes 2008](#); [Marasco & Fraternali 2011](#); [Marasco et al. 2017](#)), the flaring of gas discs can be measured directly only in highly-inclined galaxies, although this is challenging as there are degeneracies between the thickness of the discs and the inclination of galaxies, warps along the line of sight, or the presence of layers of extra-planar gas (e.g. [Kerr et al. 1957](#); [Sancisi & Allen 1979](#); [Merrifield 1992](#); [Oosterloo et al. 2007](#); [O’Brien et al. 2010](#); [Yim et al. 2014](#)). Notwithstanding, the scale height of any galaxy can also be obtained by solving the equations of vertical hydrostatic equilibrium (i.e. assuming that the gas pressure is in balance with the gravitational pull) given the galactic potential (see for instance [van der Kruit 1981](#); [Romeo 1992](#); [Olling 1995](#); [Iorio 2018](#); [Bacchini et al. 2019a, 2020b](#); [Patra 2020a,b](#)). In general, evidence shows clearly that in both dwarfs and massive late-type galaxies, the scale heights of gas discs at the outermost observed radii increase typically by a factor 2 – 10 with respect to the innermost regions, often reaching values $\gtrsim 1$ kpc.

Understanding the real geometry of gas discs has important implications for our understanding of star formation, turbulence, and feedback processes (e.g. [Romeo 1992](#); [Bacchini et al. 2019a](#); [Utomo et al. 2019](#); [Bacchini et al. 2020a](#)). The flaring of the discs can also play a role when deriving the rotation curve decomposition and mass models of galaxies. Given that the circular speed profiles of discs will depend on their gravitational potential and more specifically on the radial acceleration at the midplane, a varying scale height will produce a different circular speed than razor-thin discs and even than thick discs with constant thickness (e.g. [Binney & Tremaine 2008](#)). The effects are systematic and should be quantified.

In this paper, we aim to investigate how significantly affected mass models are when taking into account the flared geometry of the gas discs. To the best of our knowledge, the effect of gas flaring in the mass models has not been studied in the literature in a systematic way for a sample of galaxies (see e.g. [Olling 1996](#) for an individual case). So far, mass models that assume razor-thin discs have been used to derive the scale height of the H I and H₂ discs, but the impact of this on the recovered dark matter halo parameters themselves is yet to be explored. It is important to understand and quantify this, specially with the advent of large and systematic studies providing mass models. In this work, we start filling this gap by self-consistently deriving the gas flaring and dark matter halo parameters for a sample of galaxies.

Accurate computations of scale heights require detailed kinematic modelling of interferometric H I and CO data, together with robust bulge-disc decomposition. As we detailed below, we have collected such data. This also allow us to revisit important scaling relations, namely the stellar- and baryon-to-halo mass relation, and the dark matter halo concentration-mass relation. While these relations have been recently explored using mass models of large galaxy samples (e.g. [Posti et al. 2019](#); [Li et al. 2020](#)), some questions remain open. For instance, *i*) the shape of the stellar-to-halo mass relation at the lowest and highest stellar mass regime is not fully established (e.g. [Moster et al. 2013](#); [Posti et al. 2020](#)), *ii*) the baryon-to-halo mass relation remains somewhat unexplored as mass models do only rarely include both the atomic and molecular gas content, and *iii*) it has been claimed that the dark matter concentration-mass relation from N-body cosmological simulations (e.g. [Dutton & Macciò 2014](#); [Ludlow et al. 2014](#)) is not followed by the data unless imposed as a prior (e.g. [Katz et al. 2017](#); [Li et al. 2020](#)). In addition to this, it is unknown whether the flaring of the discs can affect these relations.

Gaining insight into these scaling laws is essential in the quest of understanding galaxy evolution. Besides encoding dynamical information, these relations are subject to baryonic physics and thus we can use them to constrain processes like feedback and adiabatic contraction, which are expected to impact the properties of the dark matter haloes (e.g. [Mo et al. 2010](#); [Cimatti et al. 2019](#)). We will therefore take advantage of our analysis and data to revisit these relations.

The structure of this work is as follows. In Sec. 2 we present our galaxy sample, explain its selection criteria, and describe the type of data used for each of our galaxies. In Sec. 3 we detail our methodology to derive the gas discs scale heights and mass models for each galaxy. In Sec. 4 we present our main findings, showing our mass models and scale heights. In Sec. 5 we discuss the implications of our results for the scaling relations between halo mass and concentration, stellar mass, and baryonic mass; we also discuss the main caveats of our study and compare with previous works. Finally, in Sec. 6 we summarise our main findings.

2 SAMPLE SELECTION AND DATA

To investigate the effects of the gas thickness on mass models, circular speeds, gas velocity dispersions, and mass profiles are needed. This makes it essential to select galaxies with high-quality data, mapping their gas and stellar distributions. In the case of the gas surface density profiles, deep, extended, and high-spatial resolution data (typically H I or CO emission-line observations) are needed. For the stellar component, near-IR data is desirable to trace the underlying stellar discs. Concerning the kinematics, the H I and CO data also allow to obtain the gas rotation velocity and velocity dispersion, which can then be used to obtain the circular speed. As we describe below, our sample consists of galaxies with these kind of data and with detailed kinematic models available in the literature.

2.1 Dwarf galaxies

2.1.1 Kinematics

We selected a subsample of the LITTLE THINGS galaxies ([Hunter et al. 2012](#)) studied by [Iorio et al. \(2017\)](#). Those authors provide the H I velocity dispersion (σ_{HI}) as well as the circular speed (V_c) of the galaxies after correcting the observed rotation velocities (V_{rot}) for asymmetric drift (see Sec. 4.3 in [Iorio et al. 2017](#)). These parameters¹ were derived using ^{3D}BAROLO ([Di Teodoro & Fraternali 2015](#))², a software that fits non-parametric tilted ring models to emission-line data cubes. Effectively, ^{3D}BAROLO creates 3D realizations of rotating gas discs and chooses the model that better reproduces the emission-line data, velocity channel by velocity channel, after taking into account the beam (PSF) of the observations through a convolution operation. For large disc galaxies traditional 2D methods fitting the velocity field (e.g. [de Blok et al. 2008](#); [Frank et al. 2016](#)) and ^{3D}BAROLO yield similar results. However, dwarf galaxies (and low-resolution observations in general) may suffer from beam smearing, which can significantly modify the shape of the velocity fields (e.g.

¹ All the kinematic data on LITTLE THINGS galaxies studied in [Iorio et al. \(2017\)](#) is publicly available at <https://www.filippofraternali.com/downloads>

² <https://editeodoro.github.io/Bbarolo/>

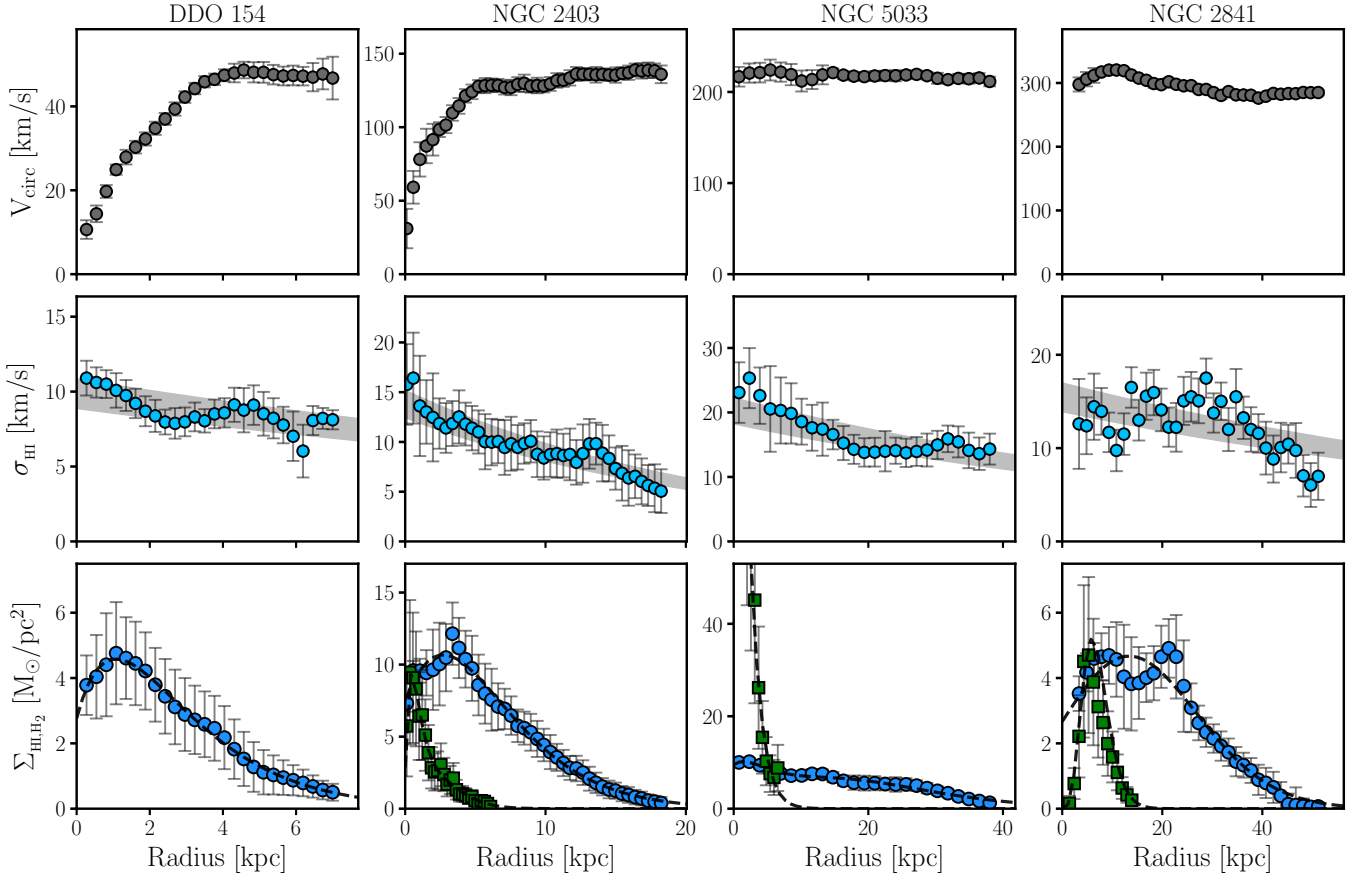


Figure 1. Data for four representative galaxies in our sample spanning our full circular speed range. *Top:* Circular speed profiles. *Middle:* H I velocity dispersion profiles. The gray band shows an exponential fit to the data (blue) with an uncertainty of ± 10 per cent in its normalisation. *Bottom:* H I (blue circles) and H₂ (green squares) surface density profiles, including helium correction. The dwarf DDO 133 has no available CO data and it likely hosts no significant H₂ reservoirs. The curves on top of the data show the functional forms fit to obtain the corresponding contributions to the total circular speed (see Sec. 3.1). In all the panels for NGC 2403 and NGC 2841 we plot one data point for every two, except for the H₂ surface density profiles.

Begeman 1987; Swaters 1999; Di Teodoro & Fraternali 2015), making 2D methods unreliable to recover the intrinsic kinematics. The 3D approach of ^{3D}BAROLO is thus mostly necessary when deriving the kinematics of dwarfs, as it largely mitigates the effects of beam smearing. Moreover, 3D methods have also the advantage of constraining simultaneously the rotation of the galaxy as well as the gas velocity dispersion.

Out of the 17 systems studied by Iorio et al. (2017), we remove the galaxies DDO 47, DDO 50, DDO 53, DDO 101, DDO 133, DDO 216, and NGC 1569. As discussed in detail by Read et al. (2017), the above galaxies are subject of concern regarding their dynamical state, distance estimation, or inclination determination, so we prefer to keep them out of our analysis, ending up with ten dwarfs. It is worth mentioning that all the galaxies have inclination angles larger than 30 degrees, which is important as uncertainties in low inclination angles translate into big uncertainties in the deprojected rotation velocities.

2.1.2 Gas and NIR optical surface densities

The H I surface densities are taken directly from Iorio et al. (2017), and we only apply a multiplicative factor of 1.36 to account for the presence of helium. Stellar 3.6 μ m surface brightness profiles are available from the S4G Survey (Bouquin et al. 2018, see also Sheth

et al. 2010) and from Zhang et al. (2012). Molecular gas is not detected in these dwarfs (e.g. Leroy et al. 2008; Bigiel et al. 2010) as it often happens with low-mass galaxies, probably due to their low metallicities (see Hunt et al. 2015 and references therein). Recently, Hunter et al. (2021) attempted to infer the molecular gas content of LITTLE THINGS galaxies based on their FUV emission. Those authors report an average H₂-to-H I fraction of about 0.2. Given that these are not direct measurements of H₂ and that the H₂-to-H I fraction of Hunter et al. (2021) is relatively small, in our analysis we do not attempt to include the molecular gas contribution in dwarf galaxies.

2.2 Spiral galaxies

2.2.1 Kinematics

To define our spiral galaxy sample, we built on the work by Di Teodoro & Peek (2021), who also used ^{3D}BAROLO to derive the H I kinematics of a sample of nearby spiral galaxies. Broadly speaking, and as detailed below, we chose their best galaxies in terms of spatial resolution, undisturbed kinematics, available bulge-disc NIR photometric decomposition, and ancillary CO observations.

Among all the galaxies from Di Teodoro & Peek (2021), we make a first selection cut and keep only those with a spatial resolution

better than 1 kpc, to ensure good sampling of the rotation curve and velocity dispersion profiles. Next, we selected against galaxies with inclinations below 30° . After this, we also eliminate the galaxies NGC 3031, NGC 3521, M83, which met the above criteria but show very perturbed kinematics or interactions with neighbors and thus it is not granted that their gas kinematics fully trace their potential wells.

Regarding the kinematics of the galaxies, we took the values from [Di Teodoro & Peek \(2021\)](#) for V_{rot}^3 and converted them to V_c following the same asymmetric drift correction prescriptions detailed in [Lorio et al. \(2017\)](#). This correction is extremely small and rather negligible for this sample of massive galaxies, but we undertook it for consistency with the LITTLE THINGS dwarfs (where the correction is significant in some cases). An additional kinematic parameter that we will need for the mass models and the derivation of the scale height of the H_2 discs is their velocity dispersion (see Section 3.2). The rotation curves of H I and H_2 (as traced by the CO line) show a very good agreement ([Frank et al. 2016](#); [Bacchini et al. 2020a](#)) between each other. In contrast, the H_2 velocity dispersion (σ_{H_2}) and σ_{HI} are not the same. [Bacchini et al. \(2020a\)](#), see also e.g. [Mogotsi et al. 2016](#)) found that the ratio between σ_{H_2} and σ_{HI} among late-type galaxies has a median value of 0.6, i.e. $\sigma_{\text{H}_2} \approx 0.6 \sigma_{\text{HI}}$. In principle, one could derive the velocity dispersion of the molecular gas from the CO data (see below). However, this would require the CO kinematic modelling and for some galaxies the CO emission is patchy and the measurement of σ_{H_2} is not well constrained and has large uncertainties. For the sake of homogeneity and to avoid these complications, we use the empirical results of [Bacchini et al. \(2020a\)](#) and we assume $\sigma_{\text{H}_2} = 0.6 \sigma_{\text{HI}}$; we have checked that reasonable variations of this equality do not impact our results on the mass models significantly.

2.2.2 Gas surface densities

The H I surface density profiles are taken from [Di Teodoro & Peek \(2021\)](#), and we apply the helium multiplicative factor of 1.36. In the case of the molecular gas, we derive H_2 profiles from a set of $\text{CO}(J = 2 - 1)$ and $\text{CO}(J = 1 - 0)$ total intensity maps; the existence of CO ancillary observations was one of the main criteria when selecting our sample. For this, we take advantage of following archival observations. The CO total intensity maps of the galaxies NGC 253, NGC 3351, NGC 3621, NGC 4535, and NGC 4536, come from the PHANGS-ALMA survey ([Leroy et al. 2021b,a](#)). The maps of NGC 2403, NGC 2841, NGC 3198, NGC 4559, NGC 4725, NGC 4736, and NGC 5055 come from the HERACLES survey ([Leroy et al. 2009](#)). The maps of NGC 5005 and NGC 5033 come from the BIMA project ([Helfer et al. 2003](#)), and of NGC 4651 and NGC 4698 from the VERTICO survey ([Brown et al. 2021](#)). The CO map of NGC 3486 comes from [Rahman et al. \(2012\)](#). As the CO map of NGC 3675 is not available, we extracted the published CO profile shown in [Young et al. \(1995\)](#) using a digitizing software ([Rohatgi et al. 2018](#)). Finally, the galaxies NGC 1313 and NGC 3992 have no significant CO detection in the available data ([Bajaja et al. 1995](#) and [Helfer et al. 2003](#), respectively) and CO data for NGC 3898 and NGC 5350 do not seem to exist. These last two galaxies have, however, high circular speeds (about 250 km/s and 185 km/s, see

Table 1) dominated in the inner regions by massive bulges and stellar discs, so we do not expect the lack of CO data to affect their rotation curve decomposition. The collected data have different sensitivity and spatial resolution, but overall they allow us to trace reasonably well the CO emission in the central regions of our sample.

Using the CO maps we build azimuthally averaged intensity maps using the same average geometric parameters as for the H I discs⁴, and we convert the CO intensities $I_{\text{CO}}^{(2-1)}$ to H_2 mass surface densities using

$$\frac{\Sigma_{\text{H}_2}}{M_\odot \text{ pc}^{-2}} = \frac{\alpha_{\text{CO}}^{(1-0)}}{M_\odot \text{ pc}^{-2}} \frac{1}{R_{21}} \frac{I_{\text{CO}}^{(2-1)}}{\text{K km/s}}, \quad (1)$$

where $\alpha_{\text{CO}}^{(1-0)}$ is the CO– H_2 conversion factor (including the helium correction factor of 1.36) and R_{21} the $\text{CO}(2 - 1)$ –to– $\text{CO}(1 - 0)$ intensity line ratio, for which we assume a value of 0.7 (see e.g. [Leroy et al. 2013](#); [Sandstrom et al. 2013](#); [Leroy et al. 2021b](#))⁵. While a handful of our galaxies have available $\alpha_{\text{CO}}^{(1-0)}$ measurements from [Sandstrom et al. \(2013\)](#), the majority of our sample does not have available $\alpha_{\text{CO}}^{(1-0)}$ values. This is not surprising given the difficulty in estimating $\alpha_{\text{CO}}^{(1-0)}$ precisely. For consistency, for all our spiral galaxies we adopt $\alpha_{\text{CO}}^{(1-0)} = 4.35$, the Milky Way reference value (e.g. [Bolatto et al. 2013](#) and references therein), which is also in reasonable agreement with the average value measured by [Sandstrom et al. \(2013\)](#) in a sample of nearby spiral galaxies. [Sandstrom et al. \(2013\)](#) also found radial variations on the $\alpha_{\text{CO}}^{(1-0)}$ of some galaxies in their sample. However, such variations are not always present nor seem to correlate significantly with other galaxy properties, and while most galaxies have somewhat lower values in the central regions, the scatter is large and trends with galactocentric distance are unclear. Given that molecular gas is not the dominant mass component of our galaxies at any radii we do not expect the potential uncertainties in $\alpha_{\text{CO}}^{(1-0)}$ to have a strong effect in our rotation curve decomposition. In fact, this has already been shown by [Frank et al. \(2016\)](#).

2.2.3 NIR surface brightness and bulge-disc decomposition

Given that the bulge component will be relevant when deriving our mass models, we refined our selection by requiring that our spiral galaxies have available bulge-disc decompositions from the S4G data coming from [Salo et al. \(2015\)](#). Those authors performed a detailed decomposition of the $3.6 \mu\text{m}$ surface brightness profiles of the galaxies fitting an exponential disc and a Sérsic profile, and we stick to their decomposition for the sake of consistency. We also select against galaxies with a significant bar or central PSF-like component as determining their kinematics and potentials can be ambiguous (e.g. NGC 4548). For three galaxies in our sample (NGC 2403, NGC 3198, NGC 3621) we do not use the S4G bulge-disc decomposition. The first and the last are not in the sample of [Salo et al. \(2015\)](#), while the fit for NGC 3198 is not satisfactory (e.g. the Sérsic index is 10, the maximum allowed value by the fitting routine of [Salo et al. 2015](#)). These three galaxies have, however, $3.6 \mu\text{m}$ S4G and optical surface brightness profiles without evidence of a bulge ([Kent 1987](#); [Muñoz-Mateos et al. 2009](#)). Because of this, and since the galaxies have

³ For a few galaxies we have removed a couple of data points near their centres where it is unclear whether there is actually emission (e.g. the centre of NGC 2841), or on the outer regions if the galaxies show a strong warp or an asymmetric rotation curve (e.g. NGC 3621).

⁴ We note that there is an excellent agreement between the geometric parameters of the H I discs ([Di Teodoro & Peek 2021](#)) and the reported values for the CO discs (e.g. [Leroy et al. 2021b](#); [Brown et al. 2021](#)).

⁵ The CO data for NGC 3486, NGC 3675, NGC 5005, and NGC 5033 are for the transition $J = 1 - 0$, and so we take $R_{21}=1$ in Eq. 1.

exquisite H I and CO data and are prototypical well-studied nearby galaxies, we include them in our final sample.

2.3 Final galaxy sample

In the end, our final sample consists of ten dwarf galaxies with $15 \lesssim V_c/(\text{km/s}) \lesssim 60$ and 22 more massive spirals with V_c as high as ~ 300 km/s. Table 1 lists our final galaxy sample, and gives the distance to the galaxies (taken from Di Teodoro & Peek 2021 and Mancera Piña et al. 2021), their morphological type taken from NED⁶, and their characteristic circular speed at the outer radii $V_{c,\text{out}}$. For the spiral galaxies this characteristic speed is computed following the algorithm of Lelli et al. (2016b, see their Eq. 1 and 2), i.e., by requiring that the circular speeds are flat within ~ 5 per cent over at least the last three measured points (but often many more points are included). The reported uncertainties correspond to the standard deviation in the values considered to estimate the flat speed. In the case of the dwarfs, where some of them have fewer than three points consistent with flat rotation, we use the mean outer velocity reported by Iorio et al. (2017). Fig. 1 shows the circular speeds, H I velocity dispersions, and gas surface densities for four representative galaxies in our sample spanning our full circular speed range.

We would like to highlight that although the galaxies in our sample have data coming from different studies, they all have the same type of data and have been analyzed with the same methods and thus the sample is fairly homogeneous: 1) the H I kinematics for all the galaxies are derived using ^{3D}BAROLO on data cubes, 2) all the H I and H₂ surface density profiles are based on azimuthal averages of H I and CO maps, and 3) all the galaxies have 3.6 μm photometry and are either bulgeless or have available bulge-disc decomposition derived with the same methodology. This sample is not complete, but as similar samples often used in the literature (e.g. Lelli et al. 2016a; Ponomareva et al. 2016; Mancera Piña et al. 2021), it is representative of the regularly rotating nearby galaxy population.

3 OBTAINING THE DISC THICKNESS AND DARK MATTER HALO

The general idea of mass modelling from rotation curve decomposition is that the observed circular speed profile V_c is the sum in quadrature of the circular speed profiles of the baryonic and dark matter components

$$V_c^2 = Y_d V_d |V_d| + Y_b V_b |V_b| + V_{\text{HI}} |V_{\text{HI}}| + V_{\text{H}_2} |V_{\text{H}_2}| + V_{\text{DM}} |V_{\text{DM}}|, \quad (2)$$

with V_d , V_b , V_{HI} , V_{H_2} , and V_{DM} the contributions to the circular speed by the stellar disc, stellar bulge, H I disc, H₂ disc, and dark-matter halo, respectively, and with Y_d (Y_b) the disc (bulge) mass-to-light ratio.

Our approach will be to fit V_c and obtain the dark matter halo by constraining V_{DM} (assuming a functional form with free parameters, see below) together with Y_d and Y_b . The key novelty with respect to previous studies is that the thickness of the gas discs is derived self-consistently using an iterative procedure (and thus changing V_{HI} and V_{H_2}). In the rest of this section we explain the general steps followed to obtain our final mass models.

Table 1. Galaxy sample used in this work. The first column gives the names of the galaxies, the second column their distance, the third column their morphological classification, and the fourth column their characteristic circular speed at the outermost radii.

Name	Distance [Mpc]	Morphology	$V_{c,\text{out}}$ [km/s]
Dwarf galaxies			
CV n I dwA	3.6 ± 0.2	Im	22 ± 4
DDO 52	10.3 ± 0.5	Im	51 ± 6
DDO 87	7.4 ± 2.2	Im	50 ± 9
DDO 126	4.9 ± 0.4	IBm	39 ± 3
DDO 154	3.7 ± 0.1	IB(s)m	47 ± 5
DDO 168	4.3 ± 0.3	IBm	56 ± 7
DDO 210	0.9 ± 0.1	IB(s)m	16 ± 10
NGC 2366	3.4 ± 0.3	SB(s)b	58 ± 5
UGC 8508	2.6 ± 0.2	IAm	34 ± 6
WLM	1.0 ± 0.1	IB(s)m	39 ± 3
Spiral galaxies			
NGC 0253	3.6 ± 0.3	SAB(s)c	198 ± 2
NGC 1313	4.2 ± 0.4	SB(s)d	127 ± 3
NGC 2403	3.2 ± 0.3	SAB(s)cd	136 ± 2
NGC 2841	14.1 ± 1.9	SA(r)b	286 ± 6
NGC 3198	13.8 ± 1.1	SB(rs)c	150 ± 3
NGC 3351	10.5 ± 0.8	SB(r)b	177 ± 4
NGC 3486	12.7 ± 2.8	SAB(r)c	155 ± 3
NGC 3621	6.7 ± 0.5	SA(s)d	145 ± 2
NGC 3675	14.4 ± 3.1	SA(s)b	213 ± 4
NGC 3898	22.1 ± 6.1	SA(s)ab	246 ± 5
NGC 3992	17.1 ± 4.7	SB(rs)bc	231 ± 3
NGC 4535	15.8 ± 1.3	SAB(s)c	225 ± 6
NGC 4536	15.2 ± 1.9	SAB(rs)bc	165 ± 4
NGC 4559	8.9 ± 0.8	SAB(rs)cd	123 ± 3
NGC 4651	16.8 ± 4.6	SA(rs)c	185 ± 3
NGC 4698	19.6 ± 4.2	SA(s)ab	214 ± 5
NGC 4725	12.4 ± 1.1	SAB(r)ab	211 ± 3
NGC 4736	4.4 ± 0.4	(R)SA(r)ab	148 ± 2
NGC 5005	18.4 ± 2.1	SAB(rs)bc	269 ± 6
NGC 5033	19.0 ± 2.7	SA(s)c	217 ± 3
NGC 5055	8.9 ± 0.7	SA(rs)bc	184 ± 6
NGC 5350	30.9 ± 5.5	SB(r)b	184 ± 2

3.1 From gas and stellar surface densities to circular speed profiles

Once the geometry and surface density of a matter component are known, its circular speed profile can be obtained from its gravitational potential. To derive the circular speed profiles from the surface densities, we use the software GALPYNAMICS⁷ (Iorio 2018). In the case of galactic discs, GALPYNAMICS computes the gravitational potential of a given mass distribution of density ρ via numerical integration of the expression (cf. Cuddeford 1993)

$$\Phi(R, z) = -\frac{2G}{\sqrt{R}} \int_{-\infty}^{\infty} dl \int_0^{\infty} du \sqrt{u} y K(\sqrt{y}) \rho(u, l), \quad (3)$$

where R and z are the radial and vertical coordinates, G is the gravitational constant, K the complete elliptical integral of the first kind,

⁶ The NASA/IPAC Extragalactic Database (NED) is operated by the Jet Propulsion Laboratory, California Institute of Technology, under contract with the National Aeronautics and Space Administration.

⁷ <https://gitlab.com/iogiul/galpynamics>

and y defined as:

$$y = \frac{2}{1+x}, \text{ with } x = \frac{R^2 + u^2 + (z-l)^2}{2Ru}. \quad (4)$$

The circular speed is then obtained from the derivative of the potential evaluated at the midplane

$$V_c^2(R) = R \left[\frac{\partial \Phi(R, z)}{\partial R} \right]_{z=0}. \quad (5)$$

In the case of a spherical distribution the value of V_c is simply $\sqrt{GM(r)/r}$. While deriving V_c for a given component, GALPYNAMICS uses functional forms to describe its surface density profile. Because of this, we fit the observed gas and stellar surface densities with functional forms as described below.

3.1.1 Dwarfs: H I distribution

The surface density profiles of the H I discs of the dwarfs are well described by a function of the form

$$\Sigma_{\text{HI}}(R) = \Sigma_{0,\text{HI}} e^{-R/R_1} (1 + R/R_2)^\alpha, \quad (6)$$

with Σ_0 , R_1 , R_2 and α the fitting parameters. This function has a characteristic shape that mimics very well the surface density profiles observed in gas-rich galaxies, which often show a plateau or central depression in the inner regions, then they increase, and then fall almost exponentially in the outskirts (e.g. [Swaters 1999](#); [Martinsson et al. 2016](#); [Wang et al. 2016](#)), as illustrated in Fig. 1 for DDO 133, NGC 2403, and NGC 2841.

Regarding the vertical distribution, while in a first step we assume the disc is razor-thin, the final scale height and its flaring are determined at the same time as the dark matter halo parameters, as we describe in Sec. 3.4.

3.1.2 Dwarfs: stellar discs

All our dwarf galaxies have stellar disc distributions that are very well fitted by exponential discs, with minimal departures. Therefore, we fit the stellar 3.6 μm profiles as exponential discs following

$$\Sigma_*(R) = \Sigma_{0,*} e^{-R/R_d}, \quad (7)$$

with $\Sigma_{0,*}$ and R_d the stellar central surface density and disc scale length, respectively.

To fully define the stellar disc distribution, we also need to specify the vertical structure. We assume that the stellar disc follows a sech^2 profile along the vertical direction, and that it has a constant thickness $z_d = 0.196 R_d^{0.633}$, as found in low-inclination star forming galaxies (e.g., [Bershady et al. 2010](#); see also [van der Kruit & Freeman 2011](#)). With this, the shape of V_d for the dwarfs is fully determined, and during our fitting technique we will obtain Y_d (i.e. its normalization). We remind the reader that there are no bulges present in our dwarfs, neither do the galaxies have significant H_2 , and thus in practice $V_b = V_{\text{H}_2} = 0$.

3.1.3 Spirals: H I and H₂ distributions

As for the dwarf galaxies, we fit some of the H I and H₂ profiles (including the helium content) of our spirals using Eq. 6. Some of the spirals, however, have gas surface density profiles with a more complex behavior. For these cases, following [Bacchini et al. \(2019a\)](#), we fit a ‘poly-exponential’ profile of third degree

$$\Sigma_{\text{HI,H}_2}(R) = \Sigma_{0,\text{pex}} e^{-R/R_{\text{pex}}} (1 + c_1 R + c_2 R^2 + c_3 R^3), \quad (8)$$

with Σ_{pex} , R_{pex} , c_1 , c_2 , c_3 the fitting parameters. The galaxies for which we use a poly-exponential fit are NGC 3621, NGC 4535, NGC 4736, and NGC 5033, in the case of H I, and NGC 2403, NGC 3198, NGC 3351, NGC 4535, NGC 4725, NGC 5005, NGC 5033, and NGC 5055, in the case of H₂.

In a similar way as for the dwarfs, the gas discs of the spirals are also assumed to be thin in a preliminary step, but their final scale heights are obtained through our main fitting routine.

3.1.4 Spirals: stellar bulge and disc

As mentioned before, most of our galaxies have bulge-disc decomposition available from [Salo et al. \(2015\)](#). Those authors used a parametric modelling software (GALFIT, [Peng et al. 2010](#)) to decompose the 3.6 μm surface brightness profiles into different components. In a few cases we have neglected the contribution (less than 5 per cent of the total flux) from a PSF-like or bar component. In particular, we chose the parametrizations using an exponential disc plus a Sérsic component. Some galaxies (NGC 3486, NGC 3675, NGC 4651, NGC 4736, NGC 5033, and NGC 5055) were modeled using two exponential discs to mimic a more complex behavior of their surface brightness profiles. We obtain the circular speed profile of our discs (up to the normalization Y_d) with GALPYNAMICS using an exponential profile (Eq. 7) with parameters coming from [Salo et al. 2015](#). In the case of NGC 2403, NGC 3198, and NGC 3621, for which have no bulge-disc decomposition but the galaxies look bulgeless, we take the S4G 3.6 μm surfaces brightness profiles from [Muñoz-Mateos et al. \(2009\)](#) and we fit two exponential discs (needed to reproduce the observed features in the profiles) following [Salo et al. \(2015\)](#). For all the galaxies with double stellar disc profiles we obtain their total V_* by summing the individual contributions in quadrature. For the vertical distribution of all the stellar discs we make the same assumptions as for the stellar component of the dwarfs, assuming a sech^2 profile and a thickness $z_d = 0.196 R_d^{0.633}$ constant with radius. For the galaxies with two exponential discs we do not assume each has their own $z_d(R_d)$ because usually one of the components has a low density and very large R_d (typically reproducing breaks/tails in surface brightness profiles). Instead, we combine both disc contributions and compute a half-light radius R_{eff} , which is then transformed into a pseudo R_d using $R_{\text{eff}} = 1.678 R_d$; we then assume this pseudo R_d when computing $z_d = 0.196 R_d^{0.633}$. We note that the use of the expression $R_{\text{eff}} = 1.678 R_d$ is not fully justified as it is only valid for exponential discs, but we consider it a reasonable mass-weighted compromise. In any case, this assumption does not alter our results below.

For the bulge components the situation is less straightforward. The Sérsic profile describes surface densities with a flat (2D) geometry, while in practice bulges are spheroidal. Taking this into account is relevant because the force generated by a flattened distribution is different (stronger in the midplane) than that of an spheroid, and thus it can affect the recovery of the best-fitting dark matter halo parameters and the computation of the gas discs scale height. To obtain a realistic bulge component we assume that the bulges in our galaxies are spherical⁸ and with a volume density described by a double power-law of the form:

$$\rho(r, z) = \frac{\rho_c}{(r/r_s)^\alpha (1 + (r/r_s))^\beta}, \quad (9)$$

⁸ We assume spherical symmetry for simplicity, but GALPYNAMICS can also deal with flattened spheroidal components.

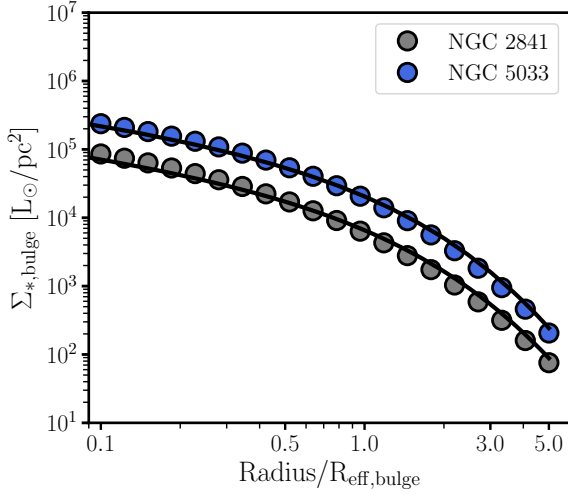


Figure 2. Comparison between the Sérsic profiles of NGC 2841 (grey) and NGC 5033 (blue) as derived by Salo et al. (2015), and the projected surface density of our best-fitting spherical bulges for those galaxies (black curves). The x-axis is normalised to the effective radii of the bulges ($R_{\text{eff}, \text{bulge}}$). We only show distances up to $5R_{\text{eff}, \text{bulge}}$ to ease the comparison, but a good agreement remains at all radii.

with $r = \sqrt{R^2 + z^2}$ the spherical radius, ρ_c and r_s a characteristic density and radius, respectively, and α and β the power-law exponents. In practice, we obtain the best set $(\rho_c, r_s, \alpha, \beta)$, using an MCMC routine based on the python package *emcee* (Foreman-Mackey et al. 2013), such that the resulting spherical bulge has a projected 2D surface density matching the Sérsic profile reported by Salo et al. (2015). The resulting bulge is then given to *GALPYNAMICS* to obtain V_b , while Υ_b is obtained during our fitting routine. Fig. 2 shows the comparison between the Sérsic profiles (circles) for the bulges of NGC 5033 and NGC 2841 and the surface density of the best-fitting spherical bulges we obtain (black curves). We find a similarly good agreement for our full sample.

3.2 Deriving the thickness and flaring of the gas discs

Given an external mass distribution (e.g. a dark matter halo and a stellar disc), *GALPYNAMICS* is able to compute the gravitational potential of an additional galaxy component (e.g. a gas disc) and estimate its scale height under the assumption of vertical hydrostatic equilibrium. This is done iteratively taking into account the external gravitational potential and the self-gravity of the additional component through an iterative process (Iorio 2018). For the interested reader, extensive and detailed discussion on the use of *GALPYNAMICS* to estimate scale heights can be found in Iorio (2018); Bacchini et al. (2019a, 2020b).

Effectively, *GALPYNAMICS* solves numerically the following expression (see Bacchini et al. 2019a; Patra 2019), which describes the 3D density profile $\rho(R, z)$ of the distribution whose scale height we aim to derive

$$\rho(R, z) = \rho(R, 0) \exp \left[-\frac{\Phi(R, z) - \Phi(R, 0)}{\sigma^2(R)} \right]. \quad (10)$$

In the above equation, $\rho(R, 0)$ is the density profile of the gas (i.e. the radial profile of its volume density) evaluated in the disc midplane. In a similar way, $\Phi(R, 0)$ is the total (dark matter plus stars plus gas disc(s)) gravitational potential $\Phi(R, z)$ evaluated in the midplane. Finally, $\sigma(R)$ is the radial profile of the gas velocity dispersion,

assumed to be isotropic. Following Bacchini et al. (2019a, 2020b), we fit the observed $\sigma(R)$ profiles with an exponential function $\sigma(R) = \sigma_0 e^{-R/R_\sigma}$, which provides a very good representation of the data and has the advantage of smoothing out small irregularities in the observed profiles, as shown in Fig. 1. The scale height $h(R)$ is defined as the standard deviation of Eq. 10, and thus it can be obtained once Φ and $\sigma(R)$ are known. Note that some authors report the scale heights as the half width at half maximum of the vertical profiles, which should then be divided by a factor 1.777 if comparing with h , as we assume a Gaussian profile for the vertical distribution. In Sec. 3.4 we explain how do we derive the thickness of the gas discs together with the best-fitting dark matter halo in a consistent way.

3.3 Fitting the dark matter halo and mass-to-light ratios

We assume that the dark matter haloes can be described by two different profiles depending on the galaxy mass. For the massive spirals we use a Navarro-Frenk-White (NFW, Navarro et al. 1997) profile, while for the dwarfs we fit the so-called CORENFW profile (Read et al. 2016a,b).

The density profile of the NFW profile is

$$\rho_{\text{NFW}}(r) = \frac{4\rho_s}{(r/r_s)(1+r/r_s)^2}, \quad (11)$$

where $r = \sqrt{R^2 + z^2}$, r_s is a scale radius, and ρ_s the volume density at r_s . This volume density can be written as

$$\rho_s = \frac{M_{200}}{16\pi r_s^3 [\ln(1+c_{200}) - c_{200}/(1+c_{200})]}, \quad (12)$$

with M_{200} the dark matter mass within a radius R_{200} where the average density is 200 times the critical density of the universe, and $c_{200} \equiv R_{200}/r_s$ is the concentration; N-body simulations find a clear anti-correlation between M_{200} and c_{200} (e.g. Dutton & Macciò 2014; Ludlow et al. 2014).

The CORENFW profile allows the classical NFW profile to develop a core if this is needed to provide a better fit to slowly rising rotation curves. This is typically the case for dwarf galaxies and the well-known cusp-core problem (see Bullock & Boylan-Kolchin 2017 for a recent review).

The density profile of the CORENFW halo is

$$\rho_{\text{coreNFW}}(r) = f^n \rho_{\text{NFW}}(r) + \frac{n f^{n-1} (1-f^2)}{4\pi r^2 r_c} M_{\text{NFW}}(r), \quad (13)$$

where ρ_{NFW} and M_{NFW} are the conventional density and mass for a NFW halo at a given radius, but $f = \tanh(r/r_c)$ is a function that generates a core of size $r_c = 2.94 R_d$. The parameter n controls how strong is the transformation from cusp to core: $n = 0$ means no core, recovering the NFW halo, and $n = 1$ means a completely cored density profile. In practice, n is defined as $n = \tanh(\kappa t_{\text{SF}}/t_{\text{dyn}})$, with $\kappa = 0.04$, t_{SF} the time whilst the galaxy has been forming stars (assumed to be 14 Gyr), and t_{dyn} the NFW dynamical time at the scale radius r_s . For further details on all these parameters we refer the reader to Read et al. (2016a,b, 2017). In the end, following the above prescriptions, the CORENFW halo has the same two free parameters as the classic NFW halo: the mass M_{200} and the concentration c_{200} .

Together with the mass-to-light ratio for the stellar disc and the bulge, the dark matter halo parameters M_{200} and c_{200} are fitted using a MCMC routine based on *emcee*. Our scripts explores the parameter

space looking for trial dark matter haloes and Y to find the best set of values to minimise Eq. 2 using χ^2 function.

For Y_d , we use a Gaussian prior centered at $Y_d = 0.5 M_\odot/L_\odot$, with a standard deviation of 0.11 dex, and with boundaries $0.1 < Y_d/(M_\odot/L_\odot) < 1.5$. Instead of fitting directly Y_b , we define a parameter f such that $Y_b = fY_d$. We impose a Gaussian prior centered on $f = 1.4$ with standard deviation of 0.1 dex and with boundaries $1 < f < 2$. These priors aim to break the degeneracy between disc, bulge, and halo in the centre of galaxies using values motivated by stellar population synthesis models (e.g. [McGaugh & Schombert 2014](#); [Meidt et al. 2014](#); [Querejeta et al. 2015](#)).

For the priors on M_{200} and c_{200} , we investigate two different scenarios. In the first one, both M_{200} and c_{200} have flat and wide priors ($8 < \log(M_{200}/M_\odot) < 14$ and $2 < c_{200} < 50$). In the second case, using the same boundary limits, we impose a Gaussian prior for c_{200} which is centered on the $c_{200} - M_{200}$ relation of [Dutton & Macciò \(2014\)](#)

$$\log(c_{200}) = 0.905 - 0.101 \log\left(\frac{0.7M_{200}}{10^{12}M_\odot}\right), \quad (14)$$

with a 1σ standard deviation of 0.11 dex and assuming a Hubble parameter $h = 0.7$. We note that our boundaries for the parameter space of c_{200} are motivated by cosmological arguments (see [McGaugh et al. 2003](#)).

The approach detailed above allows us to check whether or not the $c_{200} - M_{200}$ is recovered from the data, or if it has to be imposed to obtain physically meaningful dark matter haloes. We discuss the results of these experiments in Section 5.3.

3.4 Self-consistent derivation of the thickness and dark matter halo

We now proceed to explain how we estimate the thickness of the gas discs and the best-fitting dark matter halo for each galaxy in our sample. This is done through an iterative processes based on GALPYNAMICS and our MCMC routine. The steps are as follows.

1. Making use of GALPYNAMICS and assuming $Y_d = Y_b = 1$, V_d , V_b and the corresponding gravitational potentials Φ_d and Φ_b are derived from the stellar density profiles. We also assume that the H I and H₂ discs are razor-thin to obtain a first estimate of Φ_{HI} and Φ_{H_2} and their corresponding V_{HI} and V_{H_2} .

2. Using V_d , V_b , V_{HI} , and V_{H_2} , we fit V_c and we obtain a preliminary set $(\log(M_{200}), c_{200}, Y_d, f)$. Therefore, we can now update Φ_d and Φ_b , and obtain Φ_{DM} . Traditional rotation curve decompositions would stop here.

3. GALPYNAMICS computes the thickness of the H I disc by solving numerically Eq. 10 while taking into account Φ_{DM} , Φ_d , Φ_b , Φ_{H_2} (for a razor-thin H₂ disc) and the H I disc self-gravity. This allow us to obtain a new estimate of Φ_{HI} .

4. GALPYNAMICS computes the thickness of the H₂ disc taking into account Φ_{DM} , Φ_d , Φ_b , Φ_{HI} (derived in the previous step), and the H₂ disc self-gravity.

5. Step 3 and 4 are repeated iteratively until the changes in both scale heights, at all radii, are at least smaller than 10 per cent with respect to the previous iteration, which is a sensible choice given that the uncertainty in the scale height can be defined as the fractional error of the gas velocity dispersion ($\Delta h = h\Delta\sigma(R)/\sigma(R)$, see appendix E in [Bacchini et al. 2019a](#)), for which 10 per cent is an appropriate uncertainty (see Fig. 1). Once these iterations converge, we end up with scale heights (and Φ) for the H I and H₂ discs that were derived taking into account each other plus the stellar disc, the bulge, and the dark matter halo.

6. With all the new potentials, our MCMC routine finds a new best-fitting $(\log(M_{200}), c_{200}, Y_d, f)$ set, updating the mass model and generating a new set of potentials.

7. Steps 3 – 6 are repeated iteratively until $(\log(M_{200}), c_{200}, Y_d, f)$ converge. We adopt a convergence criterion such that the change in M_{200} , c_{200} , Y_d , and f between the last and penultimate iteration has to be less than 3 per cent. For most of our galaxies 2–3 iterations are enough to reach convergence.

Due to our iterative process, the scale height of the gas discs, the disc and bulge stellar mass-to-light ratios, and the parameters of the dark matter halo, are derived in a fully consistent way taking into account the gravitational effects of each other.

4 RESULTS

4.1 Mass models

In Fig. 3, we show the results of our rotation curve decomposition for the four representative galaxies displayed in Fig. 1. The figure corresponds to the case when c_{200} was obtained using the prior on Eq. 14. For each galaxy we show two mass models, one that assumes that the H I and H₂ (if present) discs are razor-thin as in traditional methods, and one showing our final model after taking into account the flaring of the discs. Similar plots of the mass models (and corresponding posterior distributions) for our whole sample, for both types of priors on c_{200} , are available as [supplementary material](#) to this manuscript.

We obtain successful fits for all our sample when we use a prior on the $c_{200} - M_{200}$ relation: the best-fitting V_c faithfully reproduces the observations, and the posterior distributions of the best-fitting parameters are well behaved with a Gaussian or nearly Gaussian shape. When we use the flat prior on c_{200} the fits are seemingly equally good, but for some galaxies (CVn I dwA, NGC 253, NGC 3486, NGC 3898, NGC 4535, NGC 5350, and UGC 8505) their c_{200} values are not well constrained, as their posterior distributions go towards our lower bound $c_{200} = 2$. In the following figures such galaxies are shown with different symbols to emphasise that their mass models are not fully reliable. As we discuss below, for the rest of the galaxies the mass models obtained under our two c_{200} -priors are in very good agreement with each other.

Fig. 3 shows that most of the time the overall effect of including the flaring of the gas discs is minor. This is not fully surprising: in the high-mass regime the potential of the galaxies in the inner regions is heavily dominated by the stellar components, where most of the gas mass resides. In the dwarf galaxies the gas dominates the baryonic content, but the dark matter haloes are more important from a dynamical point of view. In the case of DDO 154 (top left panel in Fig. 3), one can appreciate that by not using the razor-thin disc assumption the ‘negative’ velocities often seen in the circular speed of H I discs (e.g. [de Blok et al. 2008](#); [Frank et al. 2016](#)) are gone. While in practice those velocities are considered negative (which is why the absolute values in Eq. 2 are needed), in the presence of H I discs with a central depression, a test particle in the midplane would feel an outward acceleration due to the mass at larger radii. Because of this, the radial acceleration in the midplane is negative, and thus $|V_{HI}|V_{HI}$ is negative (see Eq. 5). Including the gas flaring strongly mitigates this effect: even when the central mass depression is there, the mass in the outer parts is distributed in a thicker disc, and thus a test particle in the midplane feels a weaker outwards acceleration, bringing $|V_{HI}|V_{HI}$ closer to zero and even to positive values. This

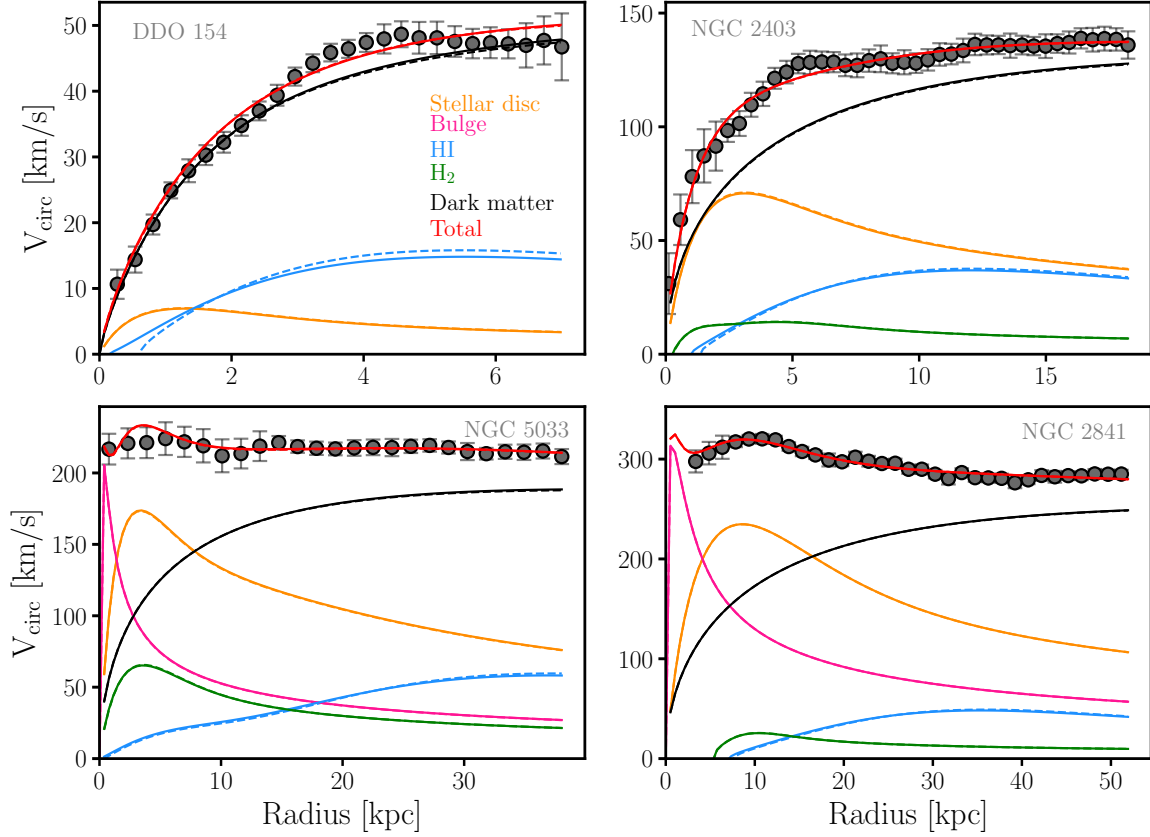


Figure 3. Mass models for the same representative galaxies as in Fig. 1. The models correspond to the case where c_{200} is obtained with a prior on Eq. 14. The points represent the circular speed profile of the galaxies (one out of each two points are shown for NGC 2403 and NGC 2841). The orange, pink, blue, green, and dark lines show the contribution to the circular speed by the stellar disc, bulge, H I disc, H₂ disc, and dark matter halo, respectively. Dashed lines show the first iteration of our MCMC (with razor-thin gas discs), while solid lines show our final model (with flared gas discs). Similar plots for all our galaxies are available as supplementary material.

is an interesting local effect only visible when considering the real geometry of the gas discs.

In a few galaxies the effects of the flaring are important. In Fig. 4 we show the mass model for the dwarf galaxy CVn I dwA, which shows the most extreme changes when including the H I disc flaring within our sample. The flaring not only gets rid of the negative $|V_{\text{HI}}|V_{\text{HI}}$ in the innermost regions, but it also decreases the contribution of the gas disc at larger radii, allowing for a dark matter halo about three times more massive.

We note here that our methodology described in Sec. 3.4 does not take into account the uncertainty in the distances of our galaxy sample. While the distance could be included as a nuisance parameter in the MCMC fitting (e.g. with a Gaussian prior, see Li et al. 2020; Mancera Piña et al. 2022), this is computationally prohibitive for our sample in our methodology as it would be required to compute the potential of each component on each iteration of the MCMC, and for each of these iterations to compute our scale heights. In practice, the distance to the galaxies tends to simply follow its prior and it only helps as a nuisance parameter to obtain appropriate uncertainties in the other quantities being fitted (see Li et al. 2020), we decided to follow a simplistic approach. We repeat our steps 1 – 7 detailed in Sec. 3.4, but assuming the upper and lower 1σ uncertainties in the distance as reported in Table 1 (note that this also implies making the appropriate changes in the surface density profiles of the baryonic components). Then, for each galaxy we combine the three posterior distributions

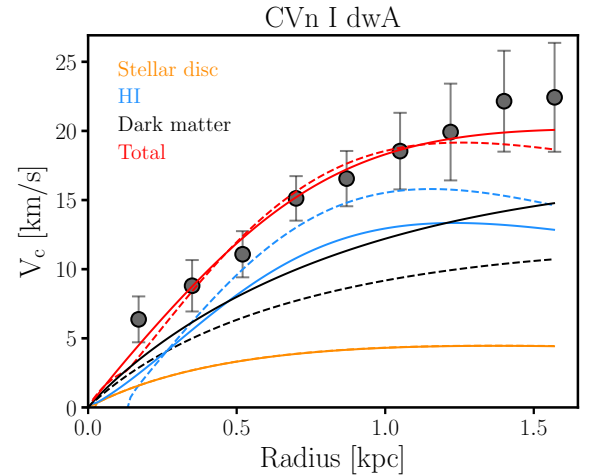


Figure 4. Mass model of the dwarf galaxy CVn I dwA. The solid (dashed) lines show the mass model when a flared (razor-thin) H I disc is used. The large effect of the flaring on the mass model is clear.

(one for each distance) of our parameters ($\log(M_{200})$, c_{200} , Y_d , f), and we re-obtain the 16th, 50th, and 84th percentiles of the final total distributions, which we use to define the final ($\log(M_{200})$, c_{200} , Y_d , f) set and its uncertainties. We report these values in Table 2 for the

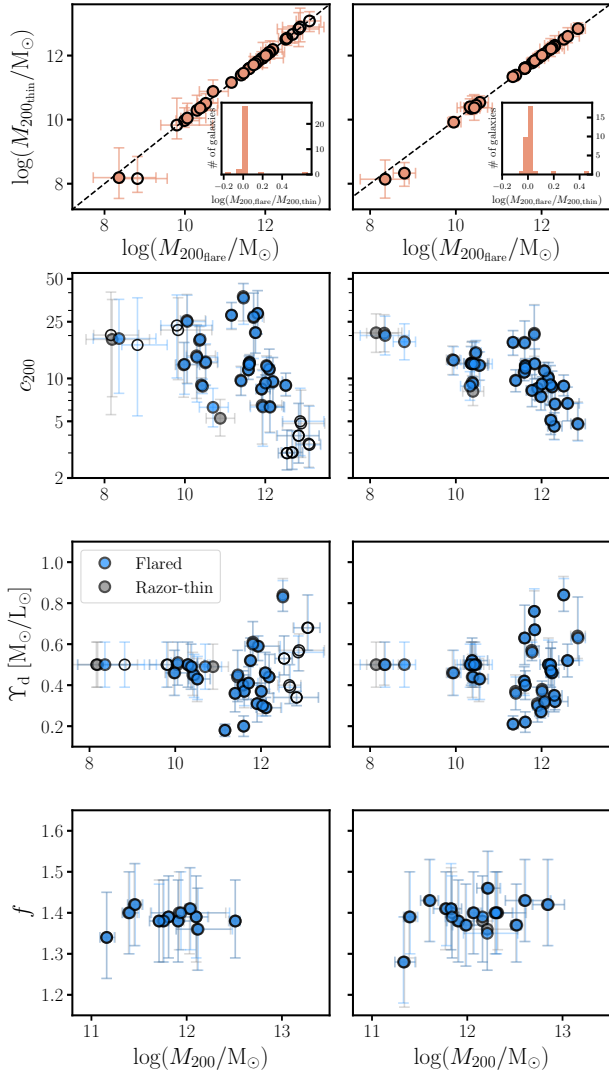


Figure 5. Comparison between the recovered parameters from our mass modelling when the gas discs are considered razor-thin (gray circles) and when the flaring is considered (blue circles); most of the time the values overlap. Empty symbols correspond to those galaxies for which we do not obtain well-constrained dark matter halo parameters when using a flat prior on c_{200} . Panels on the *left* concern the results obtained with a flat prior on c_{200} , while the *right* panels correspond to the results obtained assuming the prior on Eq. 14. The *top* panels show a direct comparison so there is no distinction between blue and grey circles; the dashed line indicates the 1:1 relation, while the insets show the distribution of the differences between M_{200} when derived with the flared and razor-thin gas discs.

case imposing the $c_{200} - M_{200}$ relation as a prior, and in Table A1 for the flat prior.

In Fig. 5 the effects of the gas flaring can be seen more clearly, as we show the comparison between the values of M_{200} , c_{200} , Y_d , and f recovered using razor-thin and flared gas discs, as a function of M_{200} . The left panels show the comparison for our uninformative prior on c_{200} while the right panel shows it for the prior on c_{200} following the $c_{200} - M_{200}$ relation of Dutton & Macciò (2014). The parameters in the figure are obtained after considering the distance uncertainty as described in the previous paragraph.

Regarding M_{200} , the values derived with both razor-thin and flared discs are compatible with the 1:1 relation. As shown in the inset, the differences between the two derivations are close to zero. The two

galaxies with a difference larger than +0.2 dex are dwarfs (the most extreme one being CVn I dwA; Fig. 4), where the flaring is expected to be more important as H I dominates the baryonic budget of the galaxies. No systematic trends as a function of M_{200} are clearly visible in the data, but this should be studied more carefully with larger samples of low-mass galaxies.

The second row of panels in Fig. 5 shows the recovered concentration parameters. Again, within the uncertainties the razor-thin- and flared-derived values are compatible. When using a flat prior, the concentration of some galaxies at high M_{200} tend towards $c_{200} = 2$, the lower limit of our priors. However, those galaxies also have low c_{200} values when imposing the prior on Eq. 14, and in general the values obtained using both priors are in agreement with each other. In Section 5.3 we discuss in detail the dark matter concentration-halo mass relation.

The third row shows the disc mass-to-light ratios. Motivated by stellar population synthesis models, we used a Gaussian prior centered at $Y_d = 0.5 \pm 0.1 M_\odot/L_\odot$. Interestingly, the values of Y_d show significant spread (which does not correlate with optical colours⁹) at $M_{200} \gtrsim 10^{11} M_\odot$ (i.e. for all the massive disc galaxies). At these masses, the median value for our flat (Eq. 14) prior scenario is 0.41 (0.46) M_\odot/L_\odot , with a standard deviation of 0.15 (0.17) M_\odot/L_\odot and values in the range 0.18 (0.21) – 0.83 (0.84) M_\odot/L_\odot . We checked with our two most extreme galaxies in terms of Y_d (NGC 2841 with $Y_d = 0.83 M_\odot/L_\odot$ and NGC 4736 with $Y_d = 0.18 M_\odot/L_\odot$) the consequences of assuming a value of $Y_d = 0.5 M_\odot/L_\odot$ often assumed when studying scaling relations (e.g. Lelli et al. 2016b; Mancera Piña et al. 2021). In the case of NGC 2841 one obtains a similar M_{200} but the fit to the rotation curve is slightly worse than in Fig. 3; moreover, the concentration of the galaxy moves away from the $c_{200} - M_{200}$ relation (see below). For NGC 4736 the mass model always overestimates the observed circular speed. This shows that the value of $Y_d = 0.5 M_\odot/L_\odot$ is representative, but for some galaxies in our sample it would bias the estimation of the stellar mass (and concentration) by a significant amount (see also the discussion in Ponomareva et al. 2018 on estimating Y_d with different methods). For smaller galaxies, Fig. 5 may give the impression that $Y_d = 0.5 M_\odot/L_\odot$ is perfectly appropriate. However, it should be noted that their posterior distributions on Y_d simply follow their Gaussian priors. This is because the contribution of V_d to the mass models of dwarfs is small, and thus our MCMC fitting loses constraining power on Y_d ; because of this, it is likely that the real uncertainties in the Y_d for the dwarfs are underestimated by 20 – 40 per cent. The effects of the gas discs flaring are negligible (up to the uncertainties just described for the dwarf galaxies), as seen from the overlap of grey and blue circles in the third panels of Fig. 5.

Finally, the bottom panels of Fig. 5 show the values of f as a function of M_{200} ; note the different range in the x-axis with respect to the other panels, as f is only a parameter for the massive galaxies with bulge. There are no visible differences between values derived with razor-thin or flared gas discs, and within the uncertainties the prior of $f = 1.4 \pm 0.1$ provides satisfactory fits to the data.

4.2 Scale heights

Fig. 6 shows the H I (blue line and band) and H₂ (green line and band) scale heights for the same four representative galaxies as before. Fig. 7 shows the scale heights for our full sample, and tables giving

⁹ We checked this by recovering the $(B - V)$ colours of our sample from the HyperLeda database (Makarov et al. 2014).

Table 2. Results of our rotation curve decomposition for the case when a prior on Eq. 14 is imposed. The columns give our fiducial values (the median of the posterior distributions) and their upper and lower uncertainties (corresponding to the 16th and 84th percentiles). Only galaxies with bulges have values of f . Note that all these quantities include the contribution from distance uncertainties.

Name	$\log(M_{200}/M_{\odot})$			c_{200}			$Y_d(M_{\odot}/L_{\odot})$			f		
	50 th pctl	$\sigma-$	$\sigma+$	50 th pctl	$\sigma-$	$\sigma+$	50 th pctl	$\sigma-$	$\sigma+$	50 th pctl	$\sigma-$	$\sigma+$
CVn I dwA	8.80	-0.26	+ 0.26	18.08	-4.57	+ 6.11	0.50	-0.11	+ 0.11	-	-	-
DDO 52	10.36	-0.16	+ 0.20	12.69	-3.18	+ 4.02	0.50	-0.11	+ 0.11	-	-	-
DDO 87	10.38	-0.19	+ 0.36	12.66	-3.74	+ 5.48	0.52	-0.11	+ 0.11	-	-	-
DDO 126	9.95	-0.14	+ 0.17	13.42	-2.85	+ 3.29	0.46	-0.11	+ 0.11	-	-	-
DDO 154	10.40	-0.08	+ 0.09	9.23	-0.95	+ 1.02	0.44	-0.11	+ 0.11	-	-	-
DDO 168	10.56	-0.16	+ 0.20	12.37	-2.64	+ 3.01	0.43	-0.11	+ 0.11	-	-	-
DDO 210	8.35	-0.57	+ 0.57	20.02	-5.42	+ 7.30	0.50	-0.11	+ 0.11	-	-	-
NGC 0253	12.31	-0.23	+ 0.30	6.60	-1.61	+ 2.01	0.32	-0.03	+ 0.03	1.40	-0.10	+ 0.10
NGC 1313	11.91	-0.12	+ 0.16	8.51	-1.41	+ 1.47	0.30	-0.08	+ 0.08	1.38	-0.10	+ 0.10
NGC 2366	10.47	-0.09	+ 0.11	15.19	-2.97	+ 3.30	0.50	-0.11	+ 0.11	-	-	-
NGC 2403	11.60	-0.05	+ 0.06	11.07	-1.40	+ 1.54	0.42	-0.07	+ 0.07	-	-	-
NGC 2841	12.52	-0.05	+ 0.05	8.81	-1.28	+ 1.69	0.84	-0.08	+ 0.08	1.37	-0.09	+ 0.09
NGC 3198	11.62	-0.02	+ 0.03	12.24	-1.36	+ 1.47	0.40	-0.07	+ 0.07	-	-	-
NGC 3351	11.78	-0.13	+ 0.16	8.22	-1.88	+ 2.36	0.56	-0.05	+ 0.05	1.41	-0.09	+ 0.09
NGC 3486	12.30	-0.15	+ 0.18	4.60	-0.89	+ 1.11	0.35	-0.08	+ 0.10	1.41	-0.10	+ 0.10
NGC 3621	11.62	-0.04	+ 0.05	11.80	-1.38	+ 1.50	0.22	-0.05	+ 0.05	-	-	-
NGC 3675	12.25	-0.13	+ 0.15	8.66	-1.86	+ 2.43	0.46	-0.10	+ 0.14	-	-	-
NGC 3898	12.85	-0.15	+ 0.17	4.76	-1.11	+ 1.89	0.63	-0.11	+ 0.19	1.42	-0.10	+ 0.11
NGC 3992	11.83	-0.05	+ 0.05	20.55	-6.41	+ 12.18	0.76	-0.10	+ 0.10	1.41	-0.10	+ 0.10
NGC 4535	12.62	-0.20	+ 0.26	6.62	-1.61	+ 1.93	0.52	-0.08	+ 0.08	1.43	-0.10	+ 0.10
NGC 4536	11.99	-0.14	+ 0.17	7.43	-1.47	+ 1.66	0.27	-0.04	+ 0.05	1.37	-0.10	+ 0.10
NGC 4559	11.41	-0.06	+ 0.07	9.63	-1.58	+ 1.81	0.36	-0.08	+ 0.08	1.39	-0.10	+ 0.10
NGC 4651	11.61	-0.09	+ 0.09	17.89	-4.53	+ 7.47	0.62	-0.13	+ 0.16	1.43	-0.10	+ 0.10
NGC 4698	12.17	-0.09	+ 0.10	10.07	-2.08	+ 2.70	0.50	-0.09	+ 0.12	1.38	-0.10	+ 0.10
NGC 4725	11.84	-0.06	+ 0.08	12.65	-2.76	+ 3.36	0.67	-0.08	+ 0.08	1.40	-0.10	+ 0.10
NGC 4736	11.33	-0.09	+ 0.12	17.97	-3.37	+ 3.72	0.21	-0.03	+ 0.03	1.28	-0.10	+ 0.10
NGC 5005	12.21	-0.24	+ 0.32	9.01	-2.51	+ 3.24	0.50	-0.06	+ 0.08	1.36	-0.09	+ 0.09
NGC 5033	12.07	-0.05	+ 0.05	11.25	-1.41	+ 1.60	0.31	-0.05	+ 0.07	1.40	-0.09	+ 0.10
NGC 5055	12.01	-0.04	+ 0.04	9.14	-1.02	+ 1.14	0.37	-0.04	+ 0.04	-	-	-
NGC 5350	12.22	-0.11	+ 0.13	5.05	-1.03	+ 1.27	0.47	-0.08	+ 0.10	1.46	-0.10	+ 0.10
UGC 8508	10.43	-0.39	+ 0.43	12.64	-3.60	+ 5.23	0.50	-0.11	+ 0.11	-	-	-
WLM	10.33	-0.22	+ 0.24	8.83	-1.80	+ 2.34	0.50	-0.11	+ 0.11	-	-	-

the scale heights are available [on-line](#). Naturally, the scale heights increase with increasing galactocentric distance. At all radii the scale height of the H I discs is larger than for the H₂ discs. This is expected given that the velocity dispersion of H I is higher.

While the overall behavior of the flaring is the same in all our galaxies, the steepness and normalization change from galaxy to galaxy (see Fig. 7). Previous observational works have postulated a ‘universality’ of the H I and H₂ scale heights in late-type galaxies when normalised to characteristic scales (Patra 2019, 2020a,b). In particular, using a sample of disc galaxies Patra (2019, 2020b) with R normalised to units of R_{25} (the radius at which a B -band isophote reaches 25 mag/arcsec²), and $h(R)$ to be unity at a radius of $0.3R_{25}$. Patra (2020a) instead adopted a pseudo-isothermal parameterisation to fit to a set of rotation curves of dwarf galaxies, and used the ‘core radius’ to normalise R . The normalised $h(R)$ values seem to have a linear dependency on the normalised radial scale, although the scatter is fairly large. The logic behind using R_{25} or the core radius is that the claimed universal shape of the $h(R)$ profiles is a dynamical effect. Thus, it is appropriate to re-scale using characteristic scales related to the radii at which the stellar or dark matter component are dominant. On the other hand using $0.3R_{25}$ as a normalization factor of $h(R)$ seems less justified.

In Fig. 7 we plot the scale heights for our galaxy sample colour-coded by the halo mass. There is a general trend of low-mass galaxies having thicker discs than their more massive counterparts, as expected given their weaker potentials. At fixed M_{200} the profiles are somewhat homogeneous, although the scatter is always large. We explore introducing the above normalizations as well as more dynamically-motivated values such as normalizing the radius to a fraction of the virial radius and the re-scale $h(R)$ according to the virial velocities, but significant scatter remains. We thus find little evidence for a universal $h(R)$ profile. This is not fully surprising as $h(R)$ depends strongly on the gas velocity dispersion, the dark matter halo, the stellar mass-to-light ratio, and the bulge-to-total mass ratio, which show a large spread in our sample. While there are a number of significant differences between the derivation of $h(R)$ by Patra (2019, 2020a,b) and ours (see for instance the discussion in Bacchini et al. 2020b), it is likely that the different conclusions arise mostly from our larger sample with a wider variety in gas kinematics, halo mass, bulge ratio, and mass-to-light ratio.

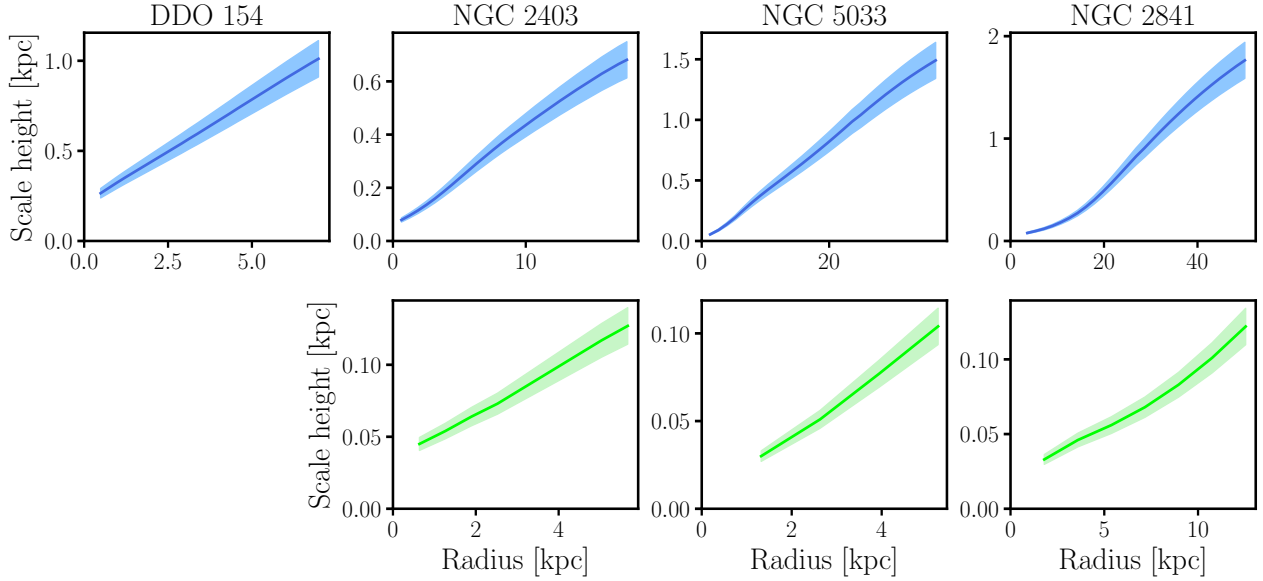


Figure 6. Example of H I (*top*) and H₂ (*bottom*) scale heights in our sample. The solid blue and green lines show our estimations, while the colour bands show the assumed uncertainty of 10 per cent, motivated by the uncertainty in the gas velocity dispersion (see Fig. 1). We only show the scale heights for our mass models with a prior on the $c_{200} - M_{200}$ relation, but the profiles obtained with the flat prior largely overlap.

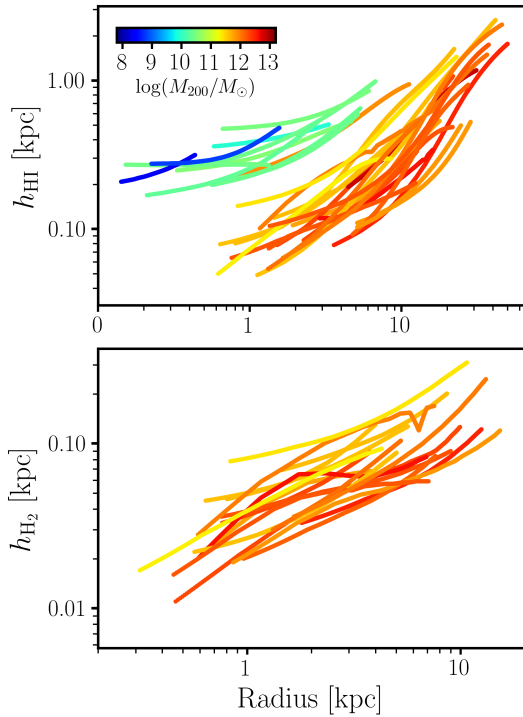


Figure 7. H I (*top*) and H₂ (*bottom*) scale heights for our galaxy sample. Galaxies are colour-coded according to their halo mass.

5 IMPLICATIONS AND DISCUSSION

Our data and the parameters we recover from our fitting procedure allow us to revisit some of the most important scaling relations concerning the connection between galaxies and their dark matter haloes. In this section, we discuss three of them: the stellar-to-halo mass relation, the baryon-to-halo mass relation, and the halo concentration-mass relation.

5.1 Stellar-to-halo mass relation

The stellar-to-halo mass relation (SHMR) has been widely studied in the context of understanding the star formation efficiency as a function of the halo mass (e.g. [Moster et al. 2013](#); [Rodríguez-Puebla et al. 2015](#); [Wechsler & Tinker 2018](#); [Posti et al. 2020](#); [Romeo 2020](#)). The classical picture based on abundance-matching techniques is that the SHMR increases monotonically from the dwarf regime till $M_* \approx 5 \times 10^{11} M_\odot$, where it flattens. The relation, however, might be different if galaxies are split in quenched and star-forming ([Rodríguez-Puebla et al. 2015](#); [Posti & Fall 2021](#)).

To compute M_* for our sample, we integrate the luminosity profiles of the bulge and disc components up to R_{200} . We do this rather than integrating to infinity in order to measure the mass of the different baryonic and dark components within the same observed radius. In any case, this integration limit has very little impact in the integrated stellar mass as the luminosity profiles have values close to zero at such large distances, and it has no repercussion on our results. Once the total luminosity of disc and bulge is estimated, we multiply by the corresponding Y_d and by fY_d in the case of the bulge, and we add the mass of both components. The uncertainties in all the quantities are estimated using Monte Carlo realizations, including distance and best-fitting parameters uncertainties. The mass of the baryonic components of our galaxies are listed in Table B1.

In the top panel of Fig. 8 we show the SHMR for our galaxy sample, using the values derived with our prior on the $c_{200} - M_{200}$ relation. The black solid lines show the cosmic limit, given by $M_{200}/f_{\text{bar,cosmic}}$. We can see that M_* increases with M_{200} rather linearly (in log-log space), although the scatter at high M_{200} is large. We compare our measurements with the abundance matching-based SHMR from [Moster et al. \(2013\)](#), and with a linear fit to the data from [Posti et al. \(2019\)](#), who performed the rotation curve decomposition of galaxies in the SPARC data base ([Lelli et al. 2016a](#)). Our data points appear to scatter around both SHMRs, but our low-number statistics prevent us from drawing conclusions on this, albeit the scatter is likely real as it is also present when studying larger samples ([Posti & Fall 2021](#)).

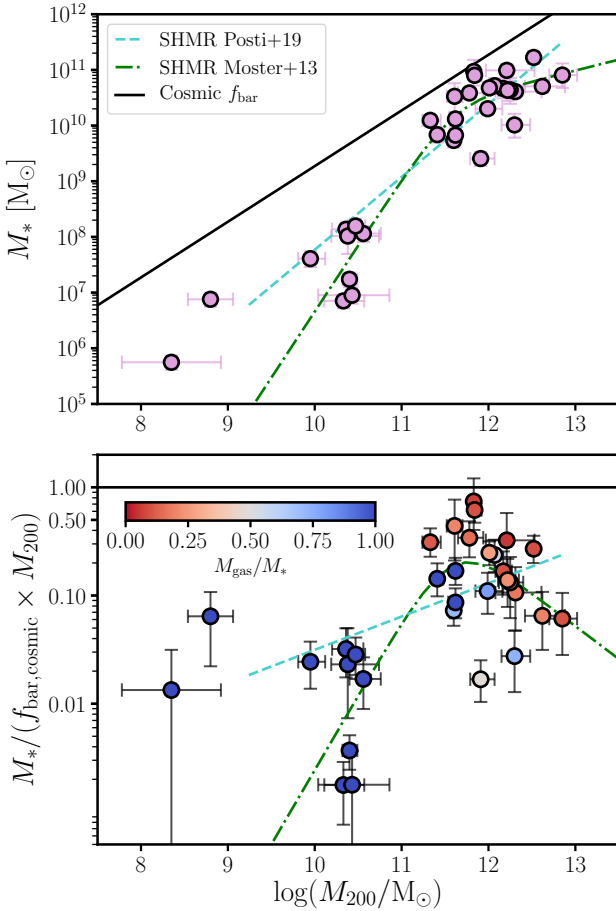


Figure 8. *Top:* Stellar-to-halo mass relation for our galaxy sample. *Bottom:* M_*/M_{200} ratio normalised to the cosmological baryon fraction vs. M_{200} . Galaxies are colour-coded according to their stellar-to-cold gas content M_{gas}/M_* . In both panels the black solid line shows the cosmological baryon fraction $f_{\text{bar,cosmic}}$. For comparison, we plot with a green semi-dashed curve the SHMR relation from [Moster et al. \(2013\)](#), while the teal dashed line shows a fit to the analysis by [Posti et al. \(2019\)](#).

In the bottom panel of Fig. 8 we show the M_*/M_{200} ratio normalised to the average cosmological baryon fraction ($f_{\text{bar,cosmic}} = \Omega_b/\Omega_m \approx 0.187$, [Planck Collaboration et al. 2020](#)). We can see that at fixed M_{200} galaxies with lower M_{gas}/M_* ratios have higher M_*/M_{200} values. In addition to this, the disc galaxies with the largest M_{200} have M_*/M_{200} as low as dwarf galaxies, despite their much lower M_{gas}/M_* . We can see from both panels that at the high-mass regime four spiral galaxies have baryon fractions between ~ 50 – 100 percent of $f_{\text{bar,cosmic}}$. The existence of galaxies with nearly all of their baryons in the form of stars at $M_* \sim 10^{11} M_\odot$ was in fact suggested recently by [Posti et al. \(2019\)](#).

To see this more clearly, in Fig. 9 we plot the stellar mass fraction now as a function of M_* . This shows that the galaxies with the highest stellar masses have also the highest M_*/M_{200} ratios. This is in qualitative agreement with the results from [Posti et al. \(2019, 2020\)](#); [Posti & Fall \(2021\)](#), and deviates significantly from the abundance-matching predictions.

5.2 Baryon-to-halo mass relation

We now focus on the baryon-to-halo mass relation (BHMR). Arguably, the BHMR is more fundamental than the SHMR, as it in-

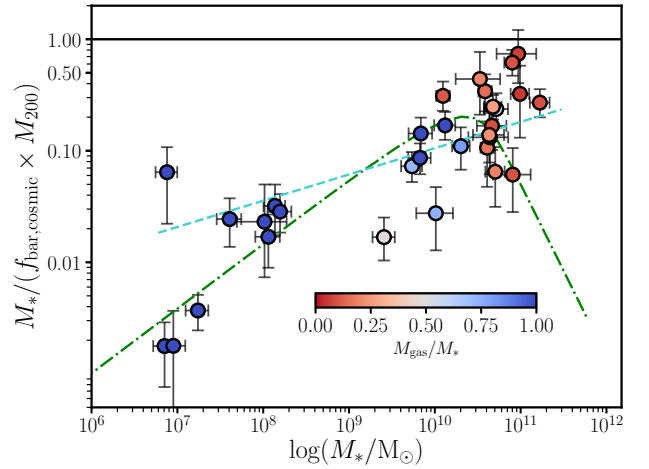


Figure 9. M_*/M_{200} ratio normalised to the cosmological baryon fraction vs. M_* . Colours and curves are as in Fig. 8.

corporates simultaneously the stellar and gas content. It is also more robust, especially at the low-mass regime since dwarf irregular galaxies are gas-dominated.

To compute the baryonic mass we consider the stellar mass as defined before, together with the neutral and molecular gas content. Similarly as for M_* , we compute M_{HI} and M_{H_2} by integrating the functional forms fitted to the observed surface densities, from 0 to R_{200} . Strictly speaking, our M_{bar} is not the total baryonic mass as it neglects the mass of the warm and hot ionised gas. This assumption is commonly made given that the warm and hot ionised gas are not expected to contribute significantly to the whole baryonic budget near galaxy discs, and because it is extremely challenging to obtain reliable mass measurements of these gas phases. Under the same logic, our M_{gas} values should be seen as the mass of the cold ISM gas.

The top panel of Fig. 10 shows the $M_{\text{bar}} - M_{200}$ relation for our galaxy sample, while the bottom panel shows the M_{bar}/M_{200} ratio normalised to the cosmic mean. Again, we show the results obtained with the prior on Eq. 14. As expected, the picture of the BHMR does not change with respect to the SHMR for the massive galaxies, dominated by the stellar component. Instead, there are substantial changes for the dwarf galaxies once their major baryonic budget is added. Overall, M_{bar}/M_{200} has significant scatter and does not show clear trends as a function of M_{200} . A similar behavior is seen in Fig. 11 but as a function of M_{bar} .

For comparison, in Figs. 10 and 11 we plot the BHMR from [Calette et al. \(2021\)](#), which is based on abundance matching to link M_* with M_{200} and in empirical correlations to link M_* to M_{gas} ; in this case they consider $M_{\text{gas}} = 1.4M_{\text{HI}}$. Predictions from similar semi-empirical approaches overlap with each other ([Rodríguez-Puebla et al. 2011](#)). The relation follows approximately the trends described by the data in the $M_{\text{bar}}/(f_{\text{bar,cosmic}} \times M_{200})$ vs. M_{200} plane, although at all M_{200} it appears to have lower M_{bar} values than most points. Similarly to what happens in the stellar relation, abundance matching does not seem to capture fully the behavior of the $M_{\text{bar}}/(f_{\text{bar,cosmic}} \times M_{200})$ vs. M_{bar} plane.

Finally, we note the peculiar position of the galaxy CVn I dwA in the above figures. At $M_{200} \approx 10^{8.8}$, CVn I dwA has a higher-than-average M_{bar}/M_{200} with a median value of about 50 per cent the cosmological baryon fraction, although the uncertainties are large.

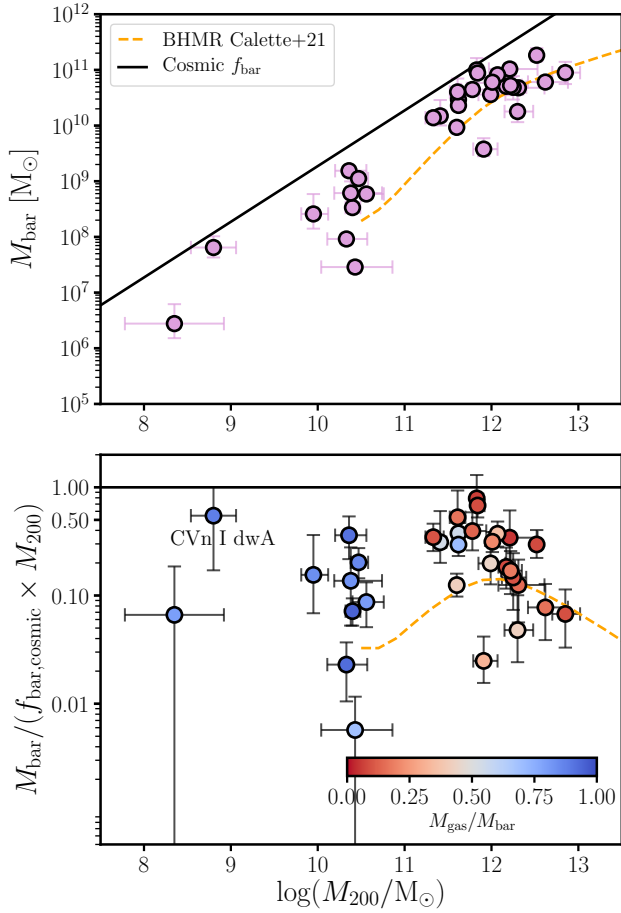


Figure 10. *Top:* Baryon-to-halo mass relation for our galaxy sample. *Bottom:* M_{bar}/M_{200} ratio normalised to the cosmological baryon fraction vs. M_{200} . Galaxies are colour-coded according to their stellar-to-cold gas content M_{gas}/M_* . In both panels the black solid line shows the cosmological baryon fraction $f_{\text{bar,cosmic}}$, and the orange dashed curve shows the semi-empirical relation from Calette et al. (2021) for comparison.

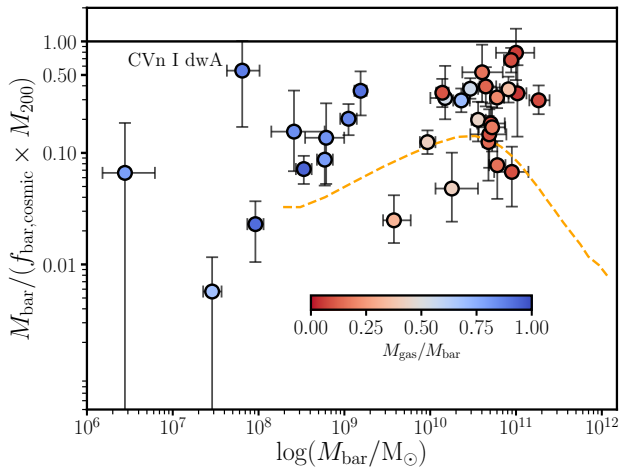


Figure 11. M_{bar}/M_{200} ratio normalised to the cosmological baryon fraction vs. M_{bar} . Colours and curves are as in Fig. 10.

CVn I dwA, is a low surface brightness dwarf with an extremely low metallicity (van Zee 2000). It would be interesting to further study this galaxy in the future, in the context of recent results that suggest the existence of a number of extended diffuse dwarf galaxies with baryon fractions comparable to the cosmological average (e.g. Mancera Piña et al. 2019, 2022).

Overall, our analysis presents empirical $M_* - M_{200}$ and $M_{\text{bar}} - M_{200}$ relations spanning five orders of magnitude in M_* , M_{bar} and M_{200} , taking into account the mass from the atomic and molecular gas, as well as the stellar disc and bulge. These relations can be used to directly test the outcome and predictions from models and simulations, setting constraints on e.g. the gas-to-stellar mass ratio, the efficiency of star formation, and the ability of galaxies to retain their baryons within their discs.

5.3 Concentration-mass relation

N-body simulations find a clear anti-correlation between M_{200} and c_{200} (e.g. Bullock et al. 2001; Dutton & Macciò 2014; Ludlow et al. 2014). Observational work on rotation curve decomposition, however, reports that this relation is not present in the data unless it is assumed as a prior during the fitting, especially when considering NFW haloes over other more flexible density profiles (see discussion in Di Cintio et al. 2014; Katz et al. 2017; Li et al. 2020 and references therein). To explore this with the best possible data, in this work we performed our rotation curve decomposition by allowing c_{200} to have 1) an uninformative flat prior, and 2) a prior following the $c_{200} - M_{200}$ of Dutton & Macciò (2014, see our Eq. 14).

In Fig. 12 we show the location of our galaxies in the $c_{200} - M_{200}$ plane, for both cases of priors on c_{200} . As mentioned before, some of our galaxies do not have a well constrained mass model when using a flat prior on c_{200} , and so we show them with crosses rather than circles; the values for these galaxies are merely indicative. We compare our measurements against the theoretical expectation from Dutton & Macciò (2014), i.e. Eq. 14.

Unsurprisingly, when Eq. 14 is imposed as a prior (left panel of Fig. 12) we recover very well the $c_{200} - M_{200}$ relation. Remarkably, even when we consider an uninformative prior on c_{200} (right panel of Fig. 12), galaxies appear to follow the $c_{200} - M_{200}$ relation albeit with larger scatter and larger individual uncertainties with respect to the case when Eq. 14 is used as a prior. Note that the galaxies for which their dark matter halo parameters are less well constrained still follow the same trends when imposing the $c_{200} - M_{200}$ relation on the left panel. Specifically, the most massive galaxies tend to deviate towards low values of c_{200} regardless of the prior.

Our results suggest that the $c_{200} - M_{200}$ relation can actually emerge from the data, provided they are of good enough quality. This is not necessarily expected given that the $c_{200} - M_{200}$ relation is obtained from cosmological N-body simulations, while baryonic physics can modify the structure of dark matter haloes. In particular, adiabatic contraction due to the baryon cooling and collapse, together with stellar/AGN feedback are expected to modify the inner density profiles (and thus the concentration) of the primordial dark matter haloes. In principle, dynamical friction between baryons and dark matter can also affect c_{200} , but its effects are expected to be minor for galaxies without extreme bars and where the baryons have retained a large fraction of their angular momentum (Sellwood 2008, see also Nipoti & Binney 2015). Since our sample was chosen not to have significant bars, and the discs have retained a large fraction of the angular momentum of the dark matter halo (Mancera Piña et al. 2021), we expect dynamical friction to be inefficient at affecting c_{200} .

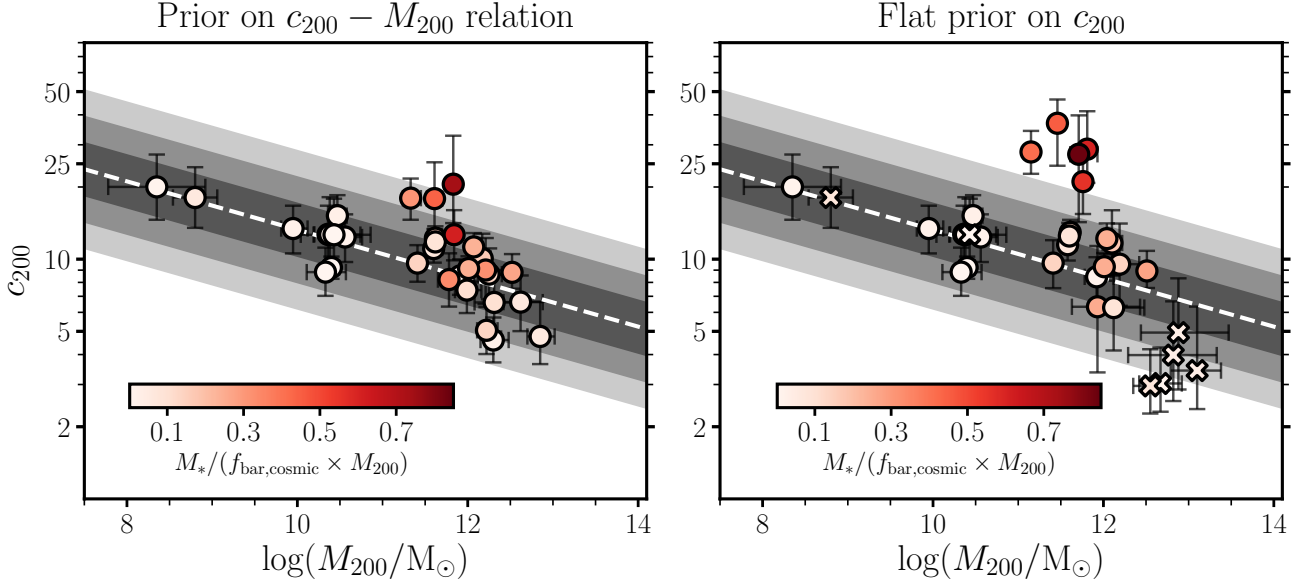


Figure 12. Concentration–mass relation for the dark matter haloes of our galaxy sample. On the *left* panel we display the results considering the prior on Eq. 14, while the *right* panel shows the results from the flat prior on c_{200} . In both panels we show the $c_{200} - M_{200}$ relation (white line) from the cosmological N-body simulations by Dutton & Macciò (2014), together with its 1, 2, 3 σ scatter (grey bands). Galaxies are colour-coded according to their $M_*/(f_{\text{bar,cosmic}} \times M_{200})$ fraction. The crosses in the right panel correspond to galaxies for which their mass models are less reliable given their posterior distributions.

significantly. Adiabatic contraction tends to increase c_{200} , since the halo contracts as response of the deeper potential owed to the central baryon condensation (e.g. Blumenthal et al. 1986; Duffy et al. 2010; Katz et al. 2014). The modification to c_{200} is not straightforward to estimate as it might depend on the individual assembly histories (e.g. Gnedin et al. 2004; Tissera et al. 2010). Feedback, on the other hand, mitigates the effects of halo contraction as it can lead to lower central dark matter densities (Navarro et al. 1996; Read & Gilmore 2005; Pontzen & Governato 2012). This is particularly true if metal-line radiative cooling is efficient (as it eases the collapse of the baryons), but the exact quantification of the effect is highly dependent on the feedback prescriptions (e.g. Sellwood 2008; Duffy et al. 2010; Bryan et al. 2013; Di Cintio et al. 2014; Katz et al. 2017).

Our results indicate that despite the above phenomena, the overall $c_{200} - M_{200}$ relation appears to hold reasonably well for most galaxies in our sample across a mass large range. Recently, Beltz-Mohrmann & Berlind (2021) analysed hydrodynamical simulations and obtained similar results. However, simulations also show that the inclusion of baryons can generate ‘wiggles’ in the $c_{200} - M_{200}$ relation due to the interplay of different feedback processes (Lovell et al. 2018; Anbajagane et al. 2022). Interestingly, such deviations seem to be present in our data, at similar M_{200} as in the simulations; namely, the higher concentrations at about $M_{200} \sim 5 \times 10^{11} M_{\odot}$ (where adiabatic contraction is efficient the most), and lower concentrations at $M_{200} \sim 10^{13} M_{\odot}$. Note that when we impose the prior of Eq. 14 on c_{200} the deviations are reduced but still present.

While the comparisons with the results of hydrodynamical simulations are complex and out of the scope of this paper, we can speculate on a qualitative explanation for the trends in our data. With this in mind, in Fig. 12 we colour-code the galaxies in terms of their M_*/M_{200} fraction normalised to $f_{\text{bar,cosmic}}$. As it turns out, the galaxies showing a systematically higher c_{200} are those with the largest M_*/M_{200} . Based on this, we argue that the galaxies with high M_*/M_{200} have larger c_{200} precisely because they converted most of their gas into stars; in fact these galaxies have M_{bar}/M_{200} fractions

comparable to the cosmological average host overall higher baryon fractions than galaxies of similar M_{200} (see Fig. 10).

Posti et al. (2019) has discussed the elevated baryon fractions in some spiral galaxies in detail, arguing for a ‘failed feedback’ scenario where feedback was not efficient enough to eject a significant amount of gas before the galaxies built their stellar mass. In the framework of adiabatic contraction, the high central stellar mass densities could then be responsible for the higher concentrations. Under this scenario, below $M_{200} \sim 5 \times 10^{11} M_{\odot}$ the effects of adiabatic contraction and stellar feedback fully compensate each other (or are both negligible). According to our figure, at $M_{200} \gtrsim 5 \times 10^{12} M_{\odot}$ it would be required that feedback overpowers halo contraction, lowering the concentration and also the global baryon- and stellar-to halo mass fractions. In fact, AGN feedback has been found to be able to lower c_{200} as well as the baryon fraction in galaxies according to simulations (e.g. Duffy et al. 2010; Bryan et al. 2013). Moreover, semi-empirical models also find that AGN feedback becomes more efficient at such masses and it manages to reproduce the SHMR (Marasco et al. 2021, see also e.g. Fabian 2012; Choi et al. 2015). Despite the scenario we sketch being merely qualitative, it seems in line with expectations of feedback processes and adiabatic contraction models. However, all this should be tested by repeating the experiment of using a flat prior on c_{200} for larger samples, and ideally complementing it with stellar rotation curves to trace at high resolution the innermost regions of the most massive galaxies, which largely determine their c_{200} parameters. In general, the above trends between M_{200} , c_{200} , and M_*/M_{200} can be exploited to further understand the connection between dark matter haloes and feedback and the build-up of mass in galaxies, providing key constraints to both analytic models and simulations.

5.4 Comparison with previous work and caveats

5.4.1 Comparison of mass models with previous works

Some galaxies in our sample have been recently studied by other authors performing standard rotation curve decomposition. Specifi-

cally, [Posti et al. \(2019\)](#) has mass models for seven of our massive galaxies and [Li et al. \(2020\)](#) for eight, while [Read et al. \(2017\)](#) studied our ten dwarfs. We find reasonably good agreement with all of their results. Below we quantify the comparison. When quoting differences, we refer to the operation of subtracting their values from ours.

First, we compare against [Posti et al. \(2019\)](#), who fitted NFW haloes using a Gaussian prior on the same $c_{200} - M_{200}$ relation as us, and a flat prior on Y_d , and $Y_b = 1.4Y_d$. Given this, for the comparison we use our results from the $c_{200} - M_{200}$ prior. Our mean (median) difference in M_{200} with respect to [Posti et al. \(2019\)](#) is 0.009 (−0.01) dex, with a standard deviation of 0.17 dex. Our mean (median) difference in c_{200} is of 0.06 (0.03) dex, with a standard deviation of 0.22 dex (mostly driven by NGC 3992 for which we find a higher c_{200} by 0.5 dex). For Y_d the mean (median) difference is −0.07 (−0.04) with a standard deviation of 0.08 dex.

Second, also for the massive galaxies, we compare our fiducial results (i.e. with the flat prior on c_{200}) with the values obtained by [Li et al. \(2020\)](#), derived using the same prior on Y_d as us, a flat prior on c_{200} , and a prior on Y_b centered at 0.7 with standard deviation of 0.1 dex (which is similar to our prior on f). Regarding M_{200} , the mean (median) difference is −0.14 (0.06) dex with a standard deviation of 0.56 dex, largely driven by NGC 5055 for which our M_{200} is 1.5 dex lower than the Li. et al. value ($0.86 \times 10^{12} M_\odot$ vs. $18.6 \times 10^{12} M_\odot$). The mean (median) difference in c_{200} is 0.06 (0.09) dex, with a standard deviation of 0.32. The mean (median) difference in Y_d is −0.03 (−0.08) dex, with standard deviation 0.09 dex. Finally, for Y_b the mean (median) difference is 0.31 (0.32) dex, with standard deviation 0.34 dex. We note here that the bulge-disc decomposition for our sample is more robust than the decomposition used in [Li et al. \(2020\)](#), which is based on a visual fit ([Lelli et al. 2016a](#)).

Lastly, we compared the results for the dwarfs against the values from [Read et al. \(2017\)](#), who used a flat prior on c_{200} and fitted M_* with a Gaussian prior with center and standard deviation according to the values by [Zhang et al. \(2012\)](#), who obtained M_* using SED fitting. The mean (median) difference in M_{200} is 0.1 (0.2) dex, with a standard deviation of 0.34 dex. There seems to be a systematic trend as a function of M_{200} , with our more massive galaxies having larger values with respect to [Read et al. \(2017\)](#), but the scatter and low number statistics do not allow to make strong conclusions. For c_{200} , the mean (median) difference is 0.1 (0.1) dex, with standard deviation 0.16 dex and our values being lower on average, without clear systematic trends. Overall, taking into account that the approaches of [Posti et al. \(2019\)](#), [Li et al. \(2020\)](#), and [Read et al. \(2017\)](#) differ significantly from ours (e.g. different rotation curves, inclinations, priors, fitting parameters, assumed geometry and shape of the stellar and gas profiles), the agreement in the recovered parameters is fairly good.

5.4.2 Caveats

Our mass models and the interpretation of our results are based on a number of assumptions. Here we focus on the two main assumptions that could affect our results the strongest: the premise of vertical hydrostatic equilibrium and the kinematic modelling on which our results rely.

Regarding the former, it is expected that regularly rotating galaxies (as those selected to be in our final sample) without recent strong interactions have their gas pressure in balance with the gravitational pull from the midplane (e.g. [Mo et al. 2010](#); [Cimatti et al. 2019](#)). Measurements in the Milky Way seem to indicate that some fraction of the atomic gas might have 50% larger scale height than expected

from hydrostatic equilibrium within ~ 5 kpc, although the agreement improves at larger radii (see [Marasco et al. 2017](#); [Bacchini et al. 2019b](#) for a detailed discussion). In general, in order to test the validity of hydrostatic equilibrium it is of primary interest to measure both the gas velocity dispersion and the gas scale height in other galaxy discs directly from observations, but there is no robust method to do so yet. Note that given our finding that the scale height influences very little the mass models except for the lowest mass galaxies, small deviations from vertical hydrostatic equilibrium would have no impact on our results regarding the SHMR, BHMR, or the $c_{200} - M_{200}$ relation.

Regarding our second assumption, one of the main motivations and strength of the paper is the argument that we self-consistently derive our mass models and scale heights taking into account each other given our iterative approach. However, the kinematic modelling from which our rotation curves and velocity dispersion profiles are derived is not consistent with the fact that gas discs are flared. The 3D kinematic modelling technique of ^{3D}BAROLO fits thin tilted-ring models ([Rogstad et al. 1974](#)) to the data cubes. This represents an improvement over fitting tilted-ring models to the velocity fields, but neither approach takes into account the increase of the scale height with radius. This is because for thick/flared discs, line of sights contain emission coming from different rings, and the ring-by-ring approach of the tilted-ring technique cannot account for this.

Despite this, the effects of assuming a thin disc when a thick disc is appropriate are known. As discussed in [Iorio \(2018\)](#) and [Di Teodoro et al. \(2019\)](#), there are three main effects due to the mixing of different disc layers in the same line of sight. By considering a thin disc instead of a thick disc: *i*) the recovered surface density profiles are shallower than in reality, *ii*) the velocity dispersion tends to be overestimated, and *iii*) the rotation velocities at large (low) radii can be slightly overestimated (underestimated). These effects are expected to be negligible for massive spiral galaxies, but somewhat more important for dwarfs, as their potential wells are shallower and their thickness are larger both in their overall value and relative to their $R_{\text{max, HI}}$ (see Fig. 7). Nevertheless, as shown by [Iorio \(2018\)](#), even for three of the least massive galaxies in our sample (DDO 210, NGC 2366, and WLM) the kinematic parameters derived with ^{3D}BAROLO are well consistent with the values estimated considering a thick disc, and the flaring is a subdominant source of uncertainty in the kinematic modelling compared to, for instance, instrumental limitations and non-circular motions. All of the above indicates that the kinematic parameters derived with the tilted-ring modelling are reliable, even if this technique cannot fully take into account the flaring of discs. In conclusion, this partial inconsistency in our methodology does not significantly affect our results.

6 CONCLUSIONS

Mass models of galaxies obtained through their rotation curve decomposition are often derived assuming that the neutral (HI) and molecular (H₂) gas discs are razor-thin. In reality, gas discs are flared, which can affect the mass models given the different gravitational effects of a flared geometry with respect to a razor-thin disc. In this paper we set out to investigate the effects of the flaring on the best-fitting parameters from rotation curve decomposition, namely the stellar mass-to-light ratios (Y), the mass of the halo (M_{200}), and its concentration (c_{200}). This is the first time that such an investigation is carried out systematically.

To this end, we use a sample of 32 late-type galaxies with the best possible data quality. Our sample has HI and CO resolved interferometric observations, bulge-disc decomposition based on deep NIR

imaging, and available 3D kinematic modelling providing their gas velocity dispersion and circular speed (V_c). The sample spans about six orders of magnitude in stellar mass (M_*), including very small ($V_c \approx 20$ km/s) and very massive ($V_c \approx 290$ km/s) galaxies. Under the assumption of vertical hydrostatic equilibrium we use an iterative approach combined with a Bayesian fitting technique to simultaneously derive the scale height of the gas discs and the mass models (using NFW and CORENFW profiles). The NFW and CORENFW profiles provide an excellent fit to the observations of our massive and dwarf galaxies, respectively. All our mass models converge with reasonable values of Y , M_{200} and c_{200} (Fig. 3). For most of our galaxies the fits are equally satisfactory by fitting c_{200} using a flat prior or by imposing a reference $c_{200} - M_{200}$ relation from N-body cosmological simulations, although for some of them the $c_{200} - M_{200}$ relation is necessary to set robust constraints on the mass models. In addition to the derivation of the gas discs flaring and the analysis of its effects, we use our detailed mass models to explore the stellar-to-halo (SHMR), baryon-to-halo (BHMR), and $c_{200} - M_{200}$ relations. Our main results can be summarised as follows.

- In the majority of our sample the effects of the flaring of the gas discs on the recovered best-fitting parameters is very minor given the larger dynamical contribution of the stellar and dark matter components. However, the effects are significant for the smallest and gas-richer dwarf galaxies, where the lower gas circular speeds of a flared disc gives room to considerably more massive haloes (Fig. 3, 4, 5).
- The scale heights of both H I and CO discs are monotonically increasing with radius in the vast majority of cases. As expected from their lower gas velocity dispersion, CO discs are considerably thinner than the H I discs. Additionally, low-mass galaxies have thicker discs than more massive ones (Fig. 6 and 7). We find little evidence of a ‘universal’ scale height profile (Fig. 7), contrary to previous claims.
- We explore the stellar-to-halo mass relation for our sample (Fig. 8). At fixed M_{200} , galaxies with higher stellar-to-gas ratios (M_*/M_{gas}) have higher M_*/M_{200} . Some galaxies around $M_{200} \approx 10^{12} M_\odot$ have very high M_*/M_{200} ratios approaching the cosmological baryon fraction, in agreement with previous findings. Nearly at all masses the galaxies scatter between a linear monotonically increasing relation and a broken power-law following abundance-matching expectations. As a function of M_* , the M_*/M_{200} ratios increase nearly monotonically (Fig. 9).
- The baryon-to-halo mass relation of our sample (Fig. 10) is similar to the stellar-to-halo mass relation at high baryonic masses (M_{bar}) but it is shallower in the low-mass regime given the high gas masses in dwarf galaxies. In general, the M_{bar}/M_{200} ratio of is more homogeneous, though with large scatter, than M_*/M_{200} (Figs. 10 and 11).
- The $c_{200} - M_{200}$ relation of our dark matter haloes follows well the expected relation from N-body cosmological simulations. This is trivial when the $c_{200} - M_{200}$ relation is imposed, but the relation appears to hold relatively well even when using an uninformative prior on c_{200} (Fig. 12). That galaxies follow the $c_{200} - M_{200}$ relation is not necessarily expected given that adiabatic contraction and feedback processes can modify the inner distribution of the dark matter density profile.
- Despite the overall $c_{200} - M_{200}$ relation being preserved, galaxies with $M_{200} \approx 5 \times 10^{11} M_\odot$ and $M_{200} \approx 10^{13} M_\odot$ seem to lie systematically above and below the relation, respectively. Interestingly, the galaxies above the relation show also the highest stellar and baryon mass fractions, opposite to the galaxies below the rela-

tion (Fig. 12). We argue that these deviations could be attributed to adiabatic contraction and AGN feedback, respectively.

We provide the largest sample for which the gas scale heights have been derived homogeneously using the hydrostatic equilibrium condition, allowing us to derive most detailed mass models. Our analysis is relevant in the context of the H I kinematics and mass modeling from the upcoming large-volume H I surveys. Moreover, our results can be directly used to test the outcome and predictions of both models and hydrodynamical simulations, with the goal of achieving a more complete picture of the physics regulating the shape of galaxies as well as the galaxy-halo connection and the efficiency of feedback processes.

ACKNOWLEDGEMENTS

We thank Heikki Salo for different clarifications on the S4G bulge-disc decomposition, and Eduardo Vitral for useful discussions regarding the reprojection of surface brightness profiles. We also thank Toby Brown for sharing with us the VERTICO data for NGC 4651 and NGC 4698, Hong-Xin Zhang for the surface brightness profile of LITTLE THINGS galaxies, Brad Frank for the comparison CO profiles of a few galaxies in our sample, and Karin Sandstrom for the α_{CO} profiles of some of our galaxies. The comments from an anonymous referee are also appreciated. P.E.M.P. and F.F. are supported by the Netherlands Research School for Astronomy (Nederlandse Onderzoekschool voor Astronomie, NOVA), research programme Network 1, Project 10.1.5.6. E.A.K.A. is supported by the WISE research programme, which is financed by the Dutch Research Council (NWO). We have used extensively SIMBAD (Wenger et al. 2000), NED, and ADS services, as well the Python packages NumPy (Oliphant 2007), Matplotlib (Hunter 2007), SciPy (Virtanen et al. 2020), and Astropy (Astropy Collaboration et al. 2018), and the tool TOPCAT (Taylor 2005) for which we are thankful.

DATA AVAILABILITY

All the data used to derive our mass models are public or available in the references and links provided in the main text. Our mass models (rotation curve decompositions and MCMC posterior distributions) and scale heights can be found [here](#). Any other data product derived from this paper is available upon request to the authors.

REFERENCES

- Anbajagane D., Evrard A. E., Farahi A., 2022, *MNRAS*, **509**, 3441
 Astropy Collaboration et al., 2018, *AJ*, **156**, 123
 Bacchini C., Fraternali F., Iorio G., Pezzulli G., 2019a, *A&A*, **622**, A64
 Bacchini C., Fraternali F., Pezzulli G., Marasco A., Iorio G., Nipoti C., 2019b, *A&A*, **632**, A127
 Bacchini C., Fraternali F., Iorio G., Pezzulli G., Marasco A., Nipoti C., 2020a, *A&A*, **641**, A70
 Bacchini C., Fraternali F., Pezzulli G., Marasco A., 2020b, *A&A*, **644**, A125
 Bajaja E., Wielebinski R., Reuter H. P., Harnett J. I., Hummel E., 1995, *A&AS*, **114**, 147
 Begeman K. G., 1987, PhD thesis, Kapteyn Astronomical Institute, University of Groningen
 Beltz-Mohrmann G. D., Berlind A. A., 2021, *ApJ*, **921**, 112
 Bershadsky M. A., Verheijen M. A. W., Westfall K. B., Andersen D. R., Swaters R. A., Martinsson T., 2010, *ApJ*, **716**, 234
 Bertone G., Hooper D., 2018, *Reviews of Modern Physics*, **90**, 045002

- Bigiel F., Leroy A., Walter F., Blitz L., Brinks E., de Blok W. J. G., Madore B., 2010, *AJ*, **140**, 1194
- Binney J., Tremaine S., 2008, *Galactic Dynamics: Second Edition*
- Blumenthal G. R., Faber S. M., Flores R., Primack J. R., 1986, *ApJ*, **301**, 27
- Bolatto A. D., Wolfire M., Leroy A. K., 2013, *ARA&A*, **51**, 207
- Bosma A., 1978, PhD thesis, -
- Bouquin A. Y. K., et al., 2018, *ApJS*, **234**, 18
- Brown T., et al., 2021, *ApJS*, **257**, 21
- Bryan S. E., Kay S. T., Duffy A. R., Schaye J., Dalla Vecchia C., Booth C. M., 2013, *MNRAS*, **429**, 3316
- Bullock J. S., Boylan-Kolchin M., 2017, *ARA&A*, **55**, 343
- Bullock J. S., Kolatt T. S., Sigad Y., Somerville R. S., Kravtsov A. V., Klypin A. A., Primack J. R., Dekel A., 2001, *MNRAS*, **321**, 559
- Calette A. R., Rodríguez-Puebla A., Avila-Reese V., Lagos C. d. P., 2021, *MNRAS*, **506**, 1507
- Choi E., Ostriker J. P., Naab T., Oser L., Moster B. P., 2015, *MNRAS*, **449**, 4105
- Cimatti A., Fraternali F., Nipoti C., 2019, *Introduction to Galaxy Formation and Evolution: From Primordial Gas to Present-Day Galaxies*. Cambridge University Press
- Cuddeford P., 1993, *MNRAS*, **262**, 1076
- Di Cintio A., Brook C. B., Macciò A. V., Stinson G. S., Knebe A., Dutton A. A., Wadsley J., 2014, *MNRAS*, **437**, 415
- Di Teodoro E. M., Fraternali F., 2015, *MNRAS*, **451**, 3021
- Di Teodoro E. M., Peek J. E. G., 2021, *ApJ*, **923**, 220
- Di Teodoro E. M., et al., 2019, *MNRAS*, **483**, 392
- Duffy A. R., Schaye J., Kay S. T., Dalla Vecchia C., Battye R. A., Booth C. M., 2010, *MNRAS*, **405**, 2161
- Dutton A. A., Macciò A. V., 2014, *MNRAS*, **441**, 3359
- Fabian A. C., 2012, *ARA&A*, **50**, 455
- Famaey B., McGaugh S. S., 2012, *Living Reviews in Relativity*, **15**, 10
- Foreman-Mackey D., Hogg D. W., Lang D., Goodman J., 2013, *PASP*, **125**, 306
- Frank B. S., de Blok W. J. G., Walter F., Leroy A., Carignan C., 2016, *AJ*, **151**, 94
- Freeman K. C., 1970, *ApJ*, **160**, 811
- Gnedin O. Y., Kravtsov A. V., Klypin A. A., Nagai D., 2004, *ApJ*, **616**, 16
- Helfer T. T., Thornley M. D., Regan M. W., Wong T., Sheth K., Vogel S. N., Blitz L., Bock D. C. J., 2003, *ApJS*, **145**, 259
- Hunt L. K., et al., 2015, *A&A*, **583**, A114
- Hunter J. D., 2007, *Computing in Science & Engineering*, **9**, 90
- Hunter D. A., et al., 2012, *AJ*, **144**, 134
- Hunter D. A., et al., 2021, *AJ*, **161**, 71
- Iorio G., 2018, PhD thesis, alma, <http://amsdottorato.unibo.it/8449/>
- Iorio G., Fraternali F., Nipoti C., Di Teodoro E., Read J. I., Battaglia G., 2017, *MNRAS*, **466**, 4159
- Kalberla P. M. W., Dedes L., 2008, *A&A*, **487**, 951
- Katz H., McGaugh S. S., Sellwood J. A., de Blok W. J. G., 2014, *MNRAS*, **439**, 1897
- Katz H., Lelli F., McGaugh S. S., Di Cintio A., Brook C. B., Schombert J. M., 2017, *MNRAS*, **466**, 1648
- Kent S. M., 1987, *AJ*, **93**, 816
- Kerr F. J., Hindman J. V., Carpenter M. S., 1957, *Nature*, **180**, 677
- Lelli F., McGaugh S. S., Schombert J. M., 2016a, *AJ*, **152**, 157
- Lelli F., McGaugh S. S., Schombert J. M., 2016b, *ApJ*, **816**, L14
- Leroy A. K., Walter F., Brinks E., Bigiel F., de Blok W. J. G., Madore B., Thornley M. D., 2008, *AJ*, **136**, 2782
- Leroy A. K., et al., 2009, *AJ*, **137**, 4670
- Leroy A. K., et al., 2013, *AJ*, **146**, 19
- Leroy A. K., et al., 2021a, *ApJS*, **255**, 19
- Leroy A. K., et al., 2021b, *ApJS*, **257**, 43
- Li P., Lelli F., McGaugh S., Schombert J., 2020, *ApJS*, **247**, 31
- Lovell M. R., et al., 2018, *MNRAS*, **481**, 1950
- Ludlow A. D., Navarro J. F., Angulo R. E., Boylan-Kolchin M., Springel V., Frenk C., White S. D. M., 2014, *MNRAS*, **441**, 378
- Makarov D., Prugniel P., Terekhova N., Courtois H., Vauglin I., 2014, *A&A*, **570**, A13
- Mancera Piña P. E., et al., 2019, *ApJ*, **883**, L33
- Mancera Piña P. E., Posti L., Fraternali F., Adams E. A. K., Oosterloo T., 2021, *A&A*, **647**, A76
- Mancera Piña P. E., Fraternali F., Oosterloo T., Adams E. A. K., Oman K. A., Leisman L., 2022, *MNRAS*, **512**, 3230
- Marasco A., Fraternali F., 2011, *A&A*, **525**, A134
- Marasco A., Fraternali F., van der Hulst J. M., Oosterloo T., 2017, *A&A*, **607**, A106
- Marasco A., Cresci G., Posti L., Fraternali F., Mannucci F., Marconi A., Belfiore F., Fall S. M., 2021, *MNRAS*, **507**, 4274
- Martinsson T. P. K., Verheijen M. A. W., Bershadsky M. A., Westfall K. B., Andersen D. R., Swaters R. A., 2016, *A&A*, **585**, A99
- McGaugh S. S., Schombert J. M., 2014, *AJ*, **148**, 77
- McGaugh S. S., de Blok W. J. G., 1998, *ApJ*, **499**, 66
- McGaugh S. S., Barker M. K., de Blok W. J. G., 2003, *ApJ*, **584**, 566
- Meidt S. E., et al., 2014, *ApJ*, **788**, 144
- Merrifield M. R., 1992, *AJ*, **103**, 1552
- Milgrom M., 1983, *ApJ*, **270**, 365
- Mo H., van den Bosch F. C., White S., 2010, *Galaxy Formation and Evolution*
- Mogotsi K. M., de Blok W. J. G., Caldú-Primo A., Walter F., Ianjamasimanana R., Leroy A. K., 2016, *AJ*, **151**, 15
- Moster B. P., Naab T., White S. D. M., 2013, *MNRAS*, **428**, 3121
- Muñoz-Mateos J. C., et al., 2009, *ApJ*, **703**, 1569
- Nakanishi H., Sofue Y., 2003, *PASJ*, **55**, 191
- Navarro J. F., Eke V. R., Frenk C. S., 1996, *MNRAS*, **283**, L72
- Navarro J. F., Frenk C. S., White S. D. M., 1997, *ApJ*, **490**, 493
- Nipoti C., Binney J., 2015, *MNRAS*, **446**, 1820
- O'Brien J. C., Freeman K. C., van der Kruit P. C., 2010, *A&A*, **515**, A62
- Oliphant T. E., 2007, *Computing in Science Engineering*, **9**, 10
- Olling R. P., 1995, *AJ*, **110**, 591
- Olling R. P., 1996, *AJ*, **112**, 481
- Oosterloo T., Fraternali F., Sancisi R., 2007, *AJ*, **134**, 1019
- Patra N. N., 2019, *MNRAS*, **484**, 81
- Patra N. N., 2020a, *MNRAS*, **495**, 2867
- Patra N. N., 2020b, *MNRAS*, **499**, 2063
- Peng C. Y., Ho L. C., Impy C. D., Rix H.-W., 2010, *AJ*, **139**, 2097
- Planck Collaboration et al., 2020, *A&A*, **641**, A6
- Ponomareva A. A., Verheijen M. A. W., Bosma A., 2016, *MNRAS*, **463**, 4052
- Ponomareva A. A., Verheijen M. A. W., Papastergis E., Bosma A., Peletier R. F., 2018, *MNRAS*, **474**, 4366
- Pontzen A., Governato F., 2012, *MNRAS*, **421**, 3464
- Posti L., Fall S. M., 2021, *A&A*, **649**, A119
- Posti L., Fraternali F., Marasco A., 2019, *A&A*, **626**, A56
- Posti L., Famaey B., Pezzulli G., Fraternali F., Ibata R., Marasco A., 2020, *A&A*, **644**, A76
- Querejeta M., et al., 2015, *ApJS*, **219**, 5
- Rahman N., et al., 2012, *ApJ*, **745**, 183
- Read J. I., Gilmore G., 2005, *MNRAS*, **356**, 107
- Read J. I., Agertz O., Collins M. L. M., 2016a, *MNRAS*, **459**, 2573
- Read J. I., Iorio G., Agertz O., Fraternali F., 2016b, *MNRAS*, **462**, 3628
- Read J. I., Iorio G., Agertz O., Fraternali F., 2017, *MNRAS*, **467**, 2019
- Ren T., Kwa A., Kaplinghat M., Yu H.-B., 2019, *Physical Review X*, **9**, 031020
- Roberts M. S., Rots A. H., 1973, *A&A*, **26**, 483
- Rodríguez-Puebla A., Avila-Reese V., Firmani C., Colín P., 2011, *Rev. Mex. Astron. Astrofis.*, **47**, 235
- Rodríguez-Puebla A., Avila-Reese V., Yang X., Foucaud S., Drory N., Jing Y. P., 2015, *ApJ*, **799**, 130
- Rogstad D. H., Lockhart I. A., Wright M. C. H., 1974, *ApJ*, **193**, 309
- Rohatgi A., Rehberg S., ZlatanStanojevic 2018, Ankitro-hatgi/Webplotdigitizer: Version 4.1 Of Webplotdigitizer, [doi:10.5281/zenodo.1137880](https://doi.org/10.5281/zenodo.1137880)
- Romeo A. B., 1992, *MNRAS*, **256**, 307
- Romeo A. B., 2020, *MNRAS*, **491**, 4843
- Rubin V. C., Ford W. K. J., Thonnard N., 1980, *ApJ*, **238**, 471
- Salo H., et al., 2015, *ApJS*, **219**, 4
- Sancisi R., Allen R. J., 1979, *A&A*, **74**, 73
- Sandstrom K. M., et al., 2013, *ApJ*, **777**, 5

- Sellwood J. A., 2008, in Funes J. G., Corsini E. M., eds, *Astronomical Society of the Pacific Conference Series Vol. 396, Formation and Evolution of Galaxy Disks*. pp 341–346 ([arXiv:0803.1574](#))
- Sheth K., et al., 2010, *PASP*, **122**, 1397
- Shostak G. S., 1973, *A&A*, **24**, 411
- Swaters R. A., 1999, PhD thesis, Kapteyn Astronomical Institute, University of Groningen
- Taylor M. B., 2005, in Shopbell P., Britton M., Ebert R., eds, *Astronomical Society of the Pacific Conference Series Vol. 347, Astronomical Data Analysis Software and Systems XIV*. p. 29
- Tissera P. B., White S. D. M., Pedrosa S., Scannapieco C., 2010, *MNRAS*, **406**, 922
- Utomo D., Blitz L., Falgarone E., 2019, *ApJ*, **871**, 17
- Virtanen P., et al., 2020, *Nature Methods*, **17**, 261
- Wang J., Koribalski B. S., Serra P., van der Hulst T., Roychowdhury S., Kamphuis P., Chengalur J. N., 2016, *MNRAS*, **460**, 2143
- Wechsler R. H., Tinker J. L., 2018, *ARA&A*, **56**, 435
- Wenger M., et al., 2000, *A&AS*, **143**, 9
- Yim K., Wong T., Xue R., Rand R. J., Rosolowsky E., van der Hulst J. M., Benjamin R., Murphy E. J., 2014, *AJ*, **148**, 127
- Young J. S., et al., 1995, *ApJS*, **98**, 219
- Zentner A., Dandavate S., Slone O., Lisanti M., 2022, *arXiv e-prints*, p. [arXiv:2202.00012](#)
- Zhang H.-X., Hunter D. A., Elmegreen B. G., Gao Y., Schruba A., 2012, *AJ*, **143**, 47
- de Blok W. J. G., Walter F., Brinks E., Trachternach C., Oh S. H., Kennicutt R. C. J., 2008, *AJ*, **136**, 2648
- van Albada T. S., Sancisi R., 1986, *Philosophical Transactions of the Royal Society of London Series A*, **320**, 447
- van Zee L., 2000, *ApJ*, **543**, L31
- van der Kruit P. C., 1981, *A&A*, **99**, 298
- van der Kruit P. C., Freeman K. C., 2011, *ARA&A*, **49**, 301

APPENDIX A: MASS MODELS WITH A FLAT PRIOR ON

C_{200}

Table A1 lists the best-fitting parameters of our rotation curve decomposition obtained using a flat prior on c_{200} .

APPENDIX B: BARYON CONTENT OF OUR GALAXY SAMPLE

Table B1 presents the estimates of the visible mass in our galaxies. The mass of the gas includes H I and H₂ (when available), while the stellar mass includes the contribution of disc and bulge (when available). The baryonic mass is the sum of the gas and stellar mass. Note that M_* has been derived using the mass-to-light ratios obtained with the prior on Eq. 14.

This paper has been typeset from a \LaTeX file prepared by the author.

Table A1. Results of our rotation curve decomposition for the case when c_{200} has a flat prior. The columns give our fiducial values (the median of the posterior distributions) and their upper and lower uncertainties (corresponding to the 16th and 84th percentiles, including the contribution from distance uncertainties. Only galaxies with bulges have values of f . Note that the posterior distributions of the galaxies CVn I dwA, DDO 210, NGC 253, NGC 3486, NGC 3898, NGC 4535, NGC 5350, and UGC 8505, are not Gaussian, and thus the reported percentiles are not as reliable as in the case of the prior on Eq. 14, but we report them here for completeness.

Name	$\log(M_{200}/M_{\odot})$			c_{200}	$\Upsilon_d(M_{\odot}/L_{\odot})$			f				
	50 th pctl	$\sigma-$	$\sigma+$		50 th pctl	$\sigma-$	$\sigma+$	50 th pctl	$\sigma-$	$\sigma+$		
CVn I dwA	8.82	-0.40	+ 0.74	17.19	-11.74	+ 19.64	0.50	-0.11	+ 0.11	-	-	-
DDO 52	10.30	-0.26	+ 0.51	14.07	-7.25	+ 9.51	0.50	-0.11	+ 0.11	-	-	-
DDO 87	10.06	-0.17	+ 0.46	25.10	-15.93	+ 13.32	0.51	-0.11	+ 0.11	-	-	-
DDO 126	9.99	-0.21	+ 0.37	12.56	-4.81	+ 5.30	0.46	-0.11	+ 0.11	-	-	-
DDO 154	10.44	-0.09	+ 0.10	8.82	-0.99	+ 1.07	0.45	-0.11	+ 0.11	-	-	-
DDO 168	10.52	-0.20	+ 0.30	13.06	-4.06	+ 4.41	0.43	-0.11	+ 0.11	-	-	-
DDO 210	8.36	-0.64	+ 0.92	19.05	-11.18	+ 16.86	0.50	-0.11	+ 0.11	-	-	-
NGC 0253	12.82	-0.53	+ 0.51	3.98	-1.42	+ 2.69	0.34	-0.03	+ 0.03	1.40	-0.10	+ 0.10
NGC 1313	11.92	-0.14	+ 0.20	8.44	-1.75	+ 1.75	0.31	-0.09	+ 0.09	1.38	-0.10	+ 0.10
NGC 2366	10.38	-0.09	+ 0.12	18.81	-4.38	+ 4.52	0.49	-0.11	+ 0.11	-	-	-
NGC 2403	11.58	-0.06	+ 0.07	11.49	-1.62	+ 1.81	0.40	-0.07	+ 0.07	-	-	-
NGC 2841	12.51	-0.06	+ 0.05	8.93	-1.35	+ 1.90	0.83	-0.07	+ 0.08	1.38	-0.09	+ 0.09
NGC 3198	11.61	-0.02	+ 0.03	12.93	-1.53	+ 1.66	0.37	-0.07	+ 0.07	-	-	-
NGC 3351	11.93	-0.30	+ 0.50	6.33	-2.96	+ 5.02	0.59	-0.06	+ 0.05	1.40	-0.09	+ 0.09
NGC 3486	12.67	-0.25	+ 0.25	3.03	-0.72	+ 1.25	0.39	-0.08	+ 0.10	1.40	-0.10	+ 0.10
NGC 3621	11.60	-0.05	+ 0.05	12.49	-1.59	+ 1.69	0.20	-0.05	+ 0.05	-	-	-
NGC 3675	12.19	-0.17	+ 0.23	9.53	-3.14	+ 4.55	0.43	-0.08	+ 0.11	-	-	-
NGC 3898	13.10	-0.31	+ 0.28	3.43	-1.06	+ 2.91	0.67	-0.11	+ 0.16	1.42	-0.11	+ 0.11
NGC 3992	11.81	-0.05	+ 0.06	28.77	-7.96	+ 12.64	0.60	-0.10	+ 0.10	1.39	-0.10	+ 0.10
NGC 4535	12.88	-0.44	+ 0.59	4.94	-2.08	+ 3.38	0.56	-0.10	+ 0.08	1.44	-0.10	+ 0.10
NGC 4536	12.12	-0.23	+ 0.36	6.28	-2.12	+ 2.34	0.29	-0.04	+ 0.05	1.36	-0.10	+ 0.10
NGC 4559	11.41	-0.07	+ 0.09	9.63	-2.06	+ 2.37	0.36	-0.09	+ 0.09	1.40	-0.10	+ 0.10
NGC 4651	11.46	-0.07	+ 0.08	36.89	-12.36	+ 9.46	0.45	-0.13	+ 0.12	1.42	-0.10	+ 0.10
NGC 4698	12.10	-0.11	+ 0.12	11.68	-3.14	+ 4.32	0.45	-0.08	+ 0.09	1.38	-0.10	+ 0.10
NGC 4725	11.76	-0.05	+ 0.06	21.06	-5.63	+ 6.07	0.51	-0.10	+ 0.10	1.38	-0.10	+ 0.10
NGC 4736	11.15	-0.07	+ 0.08	28.00	-5.30	+ 6.28	0.18	-0.03	+ 0.03	1.35	-0.10	+ 0.10
NGC 5005	11.71	-0.10	+ 0.22	27.39	-13.12	+ 12.41	0.41	-0.08	+ 0.08	1.38	-0.10	+ 0.10
NGC 5033	12.04	-0.05	+ 0.05	12.18	-1.70	+ 1.92	0.30	-0.05	+ 0.07	1.41	-0.10	+ 0.10
NGC 5055	12.01	-0.04	+ 0.04	9.30	-1.17	+ 1.31	0.37	-0.04	+ 0.04	-	-	-
NGC 5350	12.55	-0.20	+ 0.19	2.96	-0.69	+ 1.25	0.53	-0.08	+ 0.11	1.46	-0.10	+ 0.10
UGC 8508	9.80	-0.40	+ 0.88	23.54	-13.45	+ 15.03	0.50	-0.11	+ 0.11	-	-	-
WLM	10.70	-0.34	+ 0.38	6.27	-1.70	+ 2.25	0.49	-0.11	+ 0.11	-	-	-

Table B1. Stellar, gas, and baryonic (stars+gas) mass of our galaxy sample. The stellar mass has been derived using the mass-to-light ratios from our mass models considering the prior on the $c_{200} - M_{200}$ relation.

Name	$\log(M_*/M_\odot)$			$\log(M_{\text{gas}}/M_\odot)$			$\log(M_{\text{bar}}/M_\odot)$		
	50 th pctl	$\sigma-$	$\sigma+$	50 th pctl	$\sigma-$	$\sigma+$	50 th pctl	$\sigma-$	$\sigma+$
CVn I dwA	6.88	-0.13	0.12	7.76	-0.21	0.22	7.81	-0.18	0.20
DDO 52	8.14	-0.13	0.12	9.15	-0.08	0.08	9.19	-0.07	0.07
DDO 87	8.02	-0.32	0.26	8.71	-0.31	0.24	8.79	-0.25	0.21
DDO 126	7.61	-0.15	0.13	8.34	-0.34	0.40	8.41	-0.26	0.36
DDO 154	7.24	-0.14	0.12	8.50	-0.10	0.10	8.53	-0.09	0.09
DDO 168	8.06	-0.15	0.13	8.68	-0.11	0.11	8.77	-0.09	0.09
DDO 210	5.75	-0.14	0.12	6.34	-0.36	0.41	6.44	-0.26	0.35
NGC 0253	10.61	-0.08	0.08	9.85	-0.15	0.20	10.68	-0.07	0.08
NGC 1313	9.41	-0.13	0.13	9.09	-0.35	0.42	9.58	-0.13	0.20
NGC 2366	8.20	-0.15	0.13	8.98	-0.11	0.11	9.05	-0.10	0.10
NGC 2403	9.73	-0.13	0.12	9.59	-0.13	0.14	9.97	-0.09	0.09
NGC 2841	11.22	-0.12	0.11	10.21	-0.41	0.52	11.26	-0.11	0.13
NGC 3198	10.12	-0.13	0.12	10.21	-0.13	0.13	10.47	-0.09	0.09
NGC 3351	10.59	-0.08	0.08	9.77	-0.30	0.48	10.65	-0.07	0.12
NGC 3486	10.01	-0.23	0.2	9.88	-0.43	0.51	10.25	-0.19	0.30
NGC 3621	9.83	-0.14	0.12	10.21	-0.13	0.12	10.36	-0.09	0.10
NGC 3675	10.64	-0.25	0.21	9.69	-0.24	0.37	10.69	-0.22	0.20
NGC 3898	10.91	-0.23	0.21	9.93	-0.29	0.23	10.95	-0.21	0.19
NGC 3992	10.97	-0.25	0.21	9.80	-0.61	0.69	11.00	-0.23	0.21
NGC 4535	10.70	-0.11	0.11	10.00	-0.11	0.11	10.78	-0.10	0.10
NGC 4536	10.30	-0.10	0.10	10.21	-0.12	0.14	10.56	-0.08	0.09
NGC 4559	9.84	-0.14	0.13	9.91	-0.35	0.43	10.17	-0.17	0.28
NGC 4651	10.53	-0.28	0.24	9.83	-0.43	0.55	10.60	-0.23	0.24
NGC 4698	10.67	-0.18	0.17	9.65	-0.26	0.43	10.71	-0.16	0.16
NGC 4725	10.90	-0.09	0.09	9.90	-0.16	0.16	10.94	-0.08	0.09
NGC 4736	10.09	-0.08	0.08	9.15	-0.11	0.12	10.14	-0.07	0.07
NGC 5005	10.99	-0.11	0.11	9.75	-0.18	0.38	11.02	-0.10	0.11
NGC 5033	10.72	-0.14	0.14	10.47	-0.15	0.15	10.91	-0.10	0.11
NGC 5055	10.68	-0.10	0.10	10.10	-0.10	0.10	10.78	-0.08	0.08
NGC 5350	10.63	-0.19	0.17	9.98	-0.25	0.24	10.72	-0.15	0.15
UGC 8508	6.95	-0.15	0.14	7.30	-0.14	0.14	7.46	-0.10	0.11
WLM	6.85	-0.13	0.12	7.93	-0.10	0.10	7.96	-0.09	0.09